November 1998 **$** NREL/SR-520-25856

High-Efficiency Thin-Film Cadmium Telluride Photovoltaic Cells

Final Technical Report
31 January 1994–31 March 1998

A.D. Compaan and R.G. Bohn
Department of Physics and Astronomy
The University of Toledo
Toledo, Ohio

National Renewable Energy Laboratory
1617 Cole Boulevard
Golden, Colorado 80401-3393
A national laboratory of
the U.S. Department of Energy
Managed by Midwest Research Institute
for the U.S. Department of Energy
under Contract No. DE-AC36-83CH10093

NREL/SR-520-25856

High-Efficiency Thin-Film Cadmium Telluride Photovoltaic Cells

Final Technical Report
31 January 1994–31 March 1998

A.D. Compaan and R.G. Bohn
Department of Physics and Astronomy
The University of Toledo
Toledo, Ohio

NREL technical monitor: B. von Roedern

National Renewable Energy Laboratory
1617 Cole Boulevard
Golden, Colorado 80401-3393
A national laboratory of
the U.S. Department of Energy
Managed by Midwest Research Institute
for the U.S. Department of Energy
under Contract No. DE-AC36-83CH10093

Prepared under Subcontract No. ZAX-4-14013-4
November 1998

High Efficiency Thin Film Cadmium Telluride Photovoltaic Cells

Final Technical Report for the Period
January 21, 1994 to March 31, 1998

Contract No. ZAX-4-14013-4

Alvin D. Compaan, principal investigator
Randy G. Bohn, co-investigator

NREL technical monitor: B. von Roedern

Department of Physics and Astronomy
The University of Toledo
Toledo, OH 43606

High Efficiency Thin Film Cadmium Telluride Photovoltaic Cells

Final Technical Report for the Period
January 21, 1994 to March 31, 1998

Subcontract No. ZAX-4-14013-4

Alvin D. Compaan, principal investigator
Randy G. Bohn, co-investigator

Department of Physics and Astronomy
The University of Toledo
Toledo, OH 43606

NREL technical monitor: B. von Roedern

This report is available to DOE and DOE subcontractors from:
Office of Scientific and Technical Information (OSTI)
P.O. Box 62
Oak Ridge, TN 37831
Prices available by calling (423) 576-8401

Available to the public from:
National Technical Information Service (NTIS)
U.S. Department of Commerce
5285 Port Royal Road
Springfield, VA 22161
(703) 487-4650

SUMMARY

During the past year, The University of Toledo photovoltaics group has continued to develop rf sputtering for CdS/CdTe thin-film solar cells, and to work on optimizing the post-deposition process steps to match the characteristics of the sputtering process. During the fourth phase of the present contract, our work focused on efforts to determine factors which limit the efficiency in our "all-sputtered" thin-film CdTe solar cells on soda-lime glass. These issues include controlling CdS/CdTe interdiffusion, understanding the properties of the CdS_xTe_{1-x} alloy, optimizing process conditions for $CdCl_2$ treatments, manipulating the influence of ion bombardment during rf sputtering, and understanding the role of copper in quenching photoluminescence and carrier lifetimes in CdTe.

In order to improve understanding of the important CdS/CdTe interdiffusion process, we have continued our collaboration with the University at Buffalo and Brookhaven National Synchrotron Light Source in measurements using grazing incidence x-rays. Interdiffusion results in the formation of the ternary alloy material CdS_xTe_{1-x} at or near the heterojunction where its properties are critical to the operation of the solar cell. We have placed significant effort on characterizing this alloy, an effort begun in the last phase. A complete set of films spanning the alloy range, prepared by pulsed laser deposition, have now been characterized by wavelength dispersive x-ray spectroscopy and optical absorption at NREL, by Raman scattering, x-ray diffraction, and electrical measurements in our lab, and by spectroscopic ellipsometry at Brooklyn College.

We continue to participate in cooperative activity with the CdTe National Team. We prepared a series of depositions on borosilicate glass substrates having doped SnO_2 layers coated with TiO_s (prepared by the University of South Florida and Harvard) and similar substrates having a resistive SnO_2 layer on the doped tin oxide (fabricated by Golden Photon). The GPI high resistivity SnO_2 structure yielded excellent cell performance.

TABLE OF CONTENTS

LIST OF FIGURES

LIST OF TABLES

1.0 Introduction

1.1 Background

This annual report covers the fourth year of an NREL subcontract with the University of Toledo which was originally a three-year subcontract but which was extended for a fourth year and then included a no-cost extension of time to accomodate the timing of support for a graduate student working at NREL. This subcontract is focused on improvements in rf sputtering of CdS, CdTe, and related materials for thin-film solar cells on glass. In earlier work supported by NREL, the University of Toledo established the viability of rf sputtering for thin-film CdS and CdTe by fabricating "all-sputtered" cells on soda-lime glass with AM 1.5 efficiencies of up to 11.6%.[1.1,1.2,1.3] Although rf sputtered cells have not yet reached the record efficiencies of closed spaced sublimation, we believe that much of the limitation is due to process steps other than the sputtering--most importantly the back contact process.

Using the present state of the sputtering art, we have shown that the sputtering technique is advantageous in a number of ways, including the preparation of extremely thin layers and bilayers. Thus, for example, we have used sputtering to prepare 20 nm thick bilayer films of CdS/CdTe on glass for studies, at the Brookhaven National Synchrotron Light Source, of interface roughening due to annealing as measured by grazing incidence x-ray scattering and for studies of tellurium interdiffusion measured by grazing incidence x-ray fluorescence.

In addition to rf sputtering, the UT group continues to use laser physical vapor deposition (LPVD), or pulsed laser deposition (PLD), as the method of choice for the exploration of new materials such as the ternary alloys including CdS_xTe_{1-x}.

1.2 Technical Approach

RF sputtering--The process of rf sputtering permits a considerable amount of flexibility in the deposition of CdS and CdTe. It is believed that the presence of significant densities of electrons, excited atoms and ions can be manipulated to improve the quality of the as-deposited films and/or lower the growth temperature due to the impact of energetic species on the film growth interface. [1.4] Much of our effort is designed to examine these effects with the ultimate goal of fabricating rf sputtered CdS/CdTe thin film solar cells with efficiencies exceeding 15% on soda-lime glass. In order to do this, it is important to obtain a thorough understanding of the fundamentals of the sputter-deposition process. We utilize a specially designed two-gun magnetron sputtering chamber with optical thickness monitors as described previously. [1.3,1.4] As discussed in our report for last year,[1.1] this chamber is now equipped with two, type II unbalanced magnetrons, with two-inch diameter targets.

Pulsed Laser Deposition--We have continued to use PLD as a convenient method for preparation of films with unusual composition. Thus, during the past year we have prepared additional films of the ternary alloy CdS_xTe_{1-x} in response to requests from collaborators at NREL, Brooklyn College and the Univ. of Buffalo. During the past year, we have, however, moved away from dependence on PLD for the deposition of $CdCl_2$ layers prior to annealing.

Instead, we have implemented a newly constructed system for vapor $CdCl_2$ treatment and annealing of the sputtered CdS and CdTe films prior to the back contact application.

Post-Deposition Processing —For post-deposition of the sputtered films we have now standardized on a vapor $CdCl_2$ treatment and continue to adjust the parameters of temperature, time, gas composition, and gas flow to optimize the process for our films. Our standard back contact structure has been an evaporated Cu/Au but we have put into place the facilities for an aggressive search for a more robust structure in the coming year.

Characterization Tools —For characterization of films and cells, we continue to use SEM, EDS, x-ray, Raman, photoluminescence, optical absorption, Hall measurements, C-V, I-V, and SQE. We have developed extensive collaborative efforts with Case Western Reserve University for Rutherford Backscattering and XPS measurements, with University of Buffalo and Brookhaven for synchrotron x-ray measurements, and with Brooklyn College (CUNY) for ellipsometry studies. Naturally, there are several ongoing collaborations with groups at NREL.

References

1.1 A.D. Compaan, R.G. Bohn, A. Fischer, R. Wendt, D. Grecu, E. Bykov, X. Deng, C. Narayanswamy, D. Zuo, X. Ma, and K. Makhratchev, "High Efficiency Thin-Film Cadmium Telluride Photovoltaic Cells", subcontract report published in Annual Report, Photovoltaic Subcontract Program, FY1997 [available from NTIS: publication NREL/SR-520-23404 (8/97)].

1.2 A.D. Compaan, R.G. Bohn, U. Jayamaha, A. Fischer, D. Grecu, E. Bykov, C. Narayanswamy, and D. Zuo "High Efficiency Thin Film Cadmium Telluride Photovoltaic Cells," NREL Photovoltaic Program FY 1996 Annual Report [available from NTIS: publication NREL/TP-451-21233 (5/96)].

1.3 A.D. Compaan, R.G. Bohn, G. Contreras-Puente, C.N. Tabory, M. Shao, U. Jayahama, A. Fischer, Z. Feng, C. Narayanswamy, and D. Grecu, "High Efficiency Thin Film Cadmium Telluride Photovoltaic Cells," subcontract report published in Annual Report, Photovoltaic Subcontract Program, FY 1995 [available from NTIS: publication NREL/TP-451-8120 (8/95)]

1.4 M. Shao, A. Fischer, D. Grecu, U. Jayahama, E. Bykov, G. Contreras-Puente, R.G. Bohn, and A.D. Compaan, Applied Physics Letters **69**, 3045 (1996)

2.0 Studies of CdS_xTe_{1-x} alloys

During the previous phase of this project, we prepared a series of alloy films of the ternary system CdS_xTe_{1-x} with x-values (the sulfur concentration) ranging across the full alloy system. In the last annual report we discussed the results of Raman measurements of the phonon frequencies of these films. In the present phase, we have extended those Raman studies with an analysis of short range clustering and its effect on the phonon linewidth. In addition, we have sent the full range of samples to NREL where Dave Albin and Ramesh Dhere studied the optical absorption at room temperature. In our own lab we have studied the optical absorption at both room temperature and at liquid helium temperature to identify the temperature shift and to be able to separate out the phonon effects from alloy broadening effects on the near-band-edge-absorption. Our characterization of this alloy system is nearly complete at this point and we summarize below the several measurements we or collaborators have made on these films. This includes lattice constant, electrical resistivity, and phonon frequencies, which were reported in a paper at the fall-97 IEEE-PVSC meeting [2.1]. The optical fundamental gap measurements at room temperature are included courtesy of Albin and Dhere. Finally we present a discussion of the role of clustering in this alloy system as analyzed from the Raman linewidth data and presented in a paper recently published in Applied Physics Letters.

Sample preparation--Alloy films were grown using pulsed-laser-deposition (PLD) using an excimer laser operating at a wavelength of 308 nm with 80 mJ pulses at 20 Hz. The growth rate was about 0.5 nm/sec. The substrate temperature was 360°C for all the samples except for CST16 and CST17 which were grown at 275°C and 200°C, respectively. Film thickness was measured using a profilometer and ranged from 0.17 μm for CST20 to 2.13 μm for CST17. Alice Mason at NREL measured the film compositions by using wavelength dispersive x-ray spectroscopy (WDS) [3.2]. Table 2.1 shows the composition of the targets and the samples. CST16 and CST17 reflect the higher S sticking coefficient at lower temperatures when compared to CST12 which was grown at a higher temperature. The sulfur depletion seems to be greatest near the middle of the miscibility gap which extends from x = 0.06 to 0.97 at 400 ^oC [2.17]. For PLD at 360 ^oC and lower, the phase separation is kinetically limited, allowing nearly the full alloy range to be accessed.

Table 2.1: CdS_xTe_{1-x} Film Compositions

Sample ID	Target x	WDS x
CST 20	1	-
CST 22	0.9999	-
CST 23	0.99	-
CST 4	0.97	0.96
CST 5	0.94	0.90
CST 1	0.90	0.90
CST 2	0.80	0.75
CST 3	0.70	0.71
CST 17	0.60	0.48
CST 16	0.60	0.44

Sample ID	Target x	WDS x
CST 12	0.60	0.41
CST 8	0.50	0.29
CST 14	0.50	0.28
CST 13	0.40	0.20
CST 9	0.20	0.11
CST 7	0.10	0.057
CST 6	0.050	0.031
CST 10	0.020	0.017
CST 15	0.000	-

2.1 Lattice constant vs. alloy concentration

Fig. 2-1 shows some of the results of the x-ray diffraction studies of the as-grown films. The cubic <111> and hexagonal <002> have virtually the same interplanar separation. However, the cubic <311> and the hexagonal <004> reflections can be used to determine the location of the structural phase transition which, for these laser-deposited films, occurs near x = 0.45.

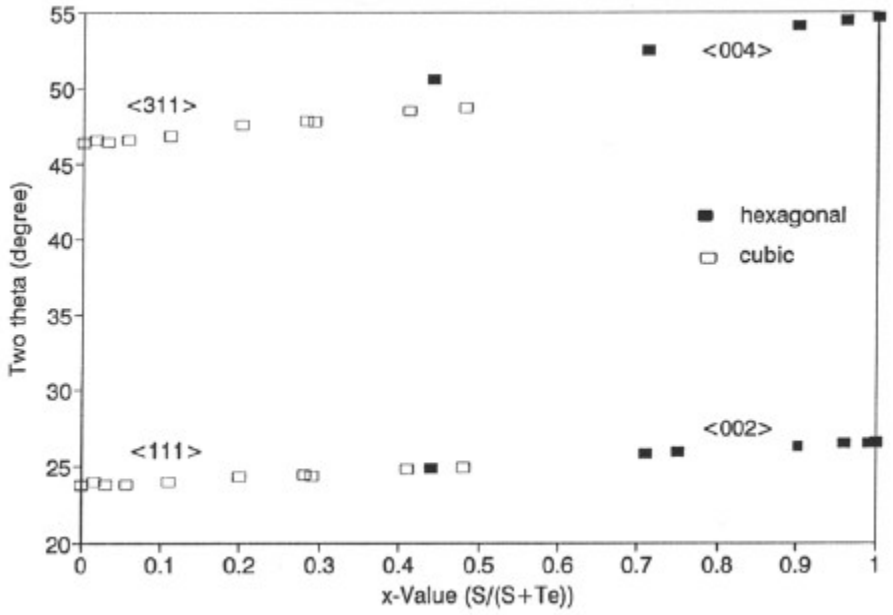

Fig. 2-1: x-ray peak positions vs S content in the alloy CdS_xTe_{1-x}.

2.2 Electrical resistivity of the CdS_xTe_{1-x} alloys

Dark resistivity--Electrical measurements were made on the as-grown films as well as on films treated with $CdCI_2$ and annealed in air at 400°C for 20 minutes. Highly resistive films were measured using a parallel stripe configuration with copper-gold contacts while the Van der Pauw/Hall technique was used for the lower resistivity films. Fig. 2-2 shows the dark resistivity at room temperature for the as-grown films. There is a strong compositional dependence with the resistivity ranging from 1000 MΩ-cm for x=0 to less than 1Ω-cm for x close to 1. The resistivity values for x=0 and x=1are consistent with the values obtained for pure CdS and CdTe that we have grown previously using PLD. From the results of the Hall measurements that were performed on selected samples, it is clear that the change in

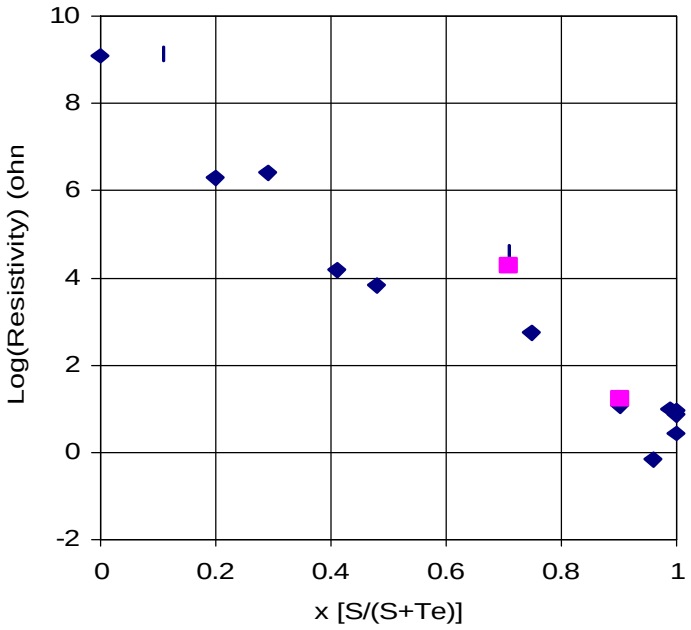

Fig. 2-2: Dark resistivity at room temperature versus x for CdS_xTe_{1-x} alloy films. Diamonds: original measurement; squares; second measurement from same deposition

carrier density (n) is primarily responsible for the change in the resistivity. For small x values (CdS-like), n is in the range of $10^{18} – 10^{19}$ /cm^3 while the mobility is low, typically of the order of 3 cm^2/V-s, or less. This can be compared to samples near x =0.3, where the carrier density is of the order of 10^{11} /cm^3 and the mobility is around 10 cm^2/V-s. All samples measured for x > 0.3 were n-type. We were not able to obtain reliable Hall measurements for x < 0.2, so the point where carrier-type conversion takes place could not be determined. However, earlier hot-probe measurements gave indications that the type conversion takes place in the vicinity of x = 0.2 for these laser-grown films.

Activation energies for the resistivities were measured for the as-grown films between 300K and 350K and are shown in Fig. 2-3 as a function of x. While this is over a limited temperature range, the data might provide some insight into the conduction mechanism in these films. The data follow a linear trend as a function of concentration with x = 1 having an activation energy of the order of 0.1 eV and x = 0 having an activation energy of the order of 0.6 eV. For x > 0.9, the activation energies for the mobility are typically less than 0.05 eV, although the uncertainties are relatively large because of the low mobilities for these samples. Orton [2.3] has developed a model for polycrystalline CdS. In this model, the grains are approximated as cylinders with traps at the grain boundaries. The temperature dependence of the conductivity, mobility, and the carrier density follows an activation energy-type behavior that depends on the degree of depletion of the grain. If the activation energy for the mobility is zero (or small), then the carrier density is approximately the same as the doping level and the intergrain barrier height is small. The grains are partially depleted and the potential barriers at the grain boundaries are narrow. For x between 0.9 and 0.4 the mobility activation energy increases to

around 0.1 eV and the carrier density decreases and is less than the doping level as the grains become more depleted. If we calculate the doping level in this region using Orton's model, we find that for $\varepsilon \approx 11$ and a grain radius of about 0.1 μm, that the doping level is about 10^{16} /cm^3 . In this concentration range the carrier densities are all less than this estimate which tends to

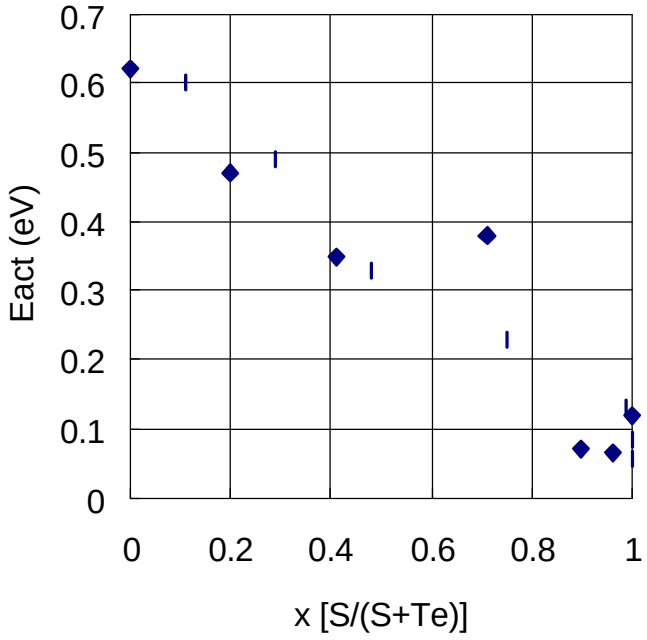

Fig. 2-3: Activation energies for the as-grown alloys

support this interpretation. The model also indicates that the activation energy for the resistivity should be the effective trap depth. This would seem to indicate that as the alloy becomes more CdTe-like, the effective trap depth increases. An energy of 0.6 eV for CdTe is not inconsistent with trap energies in the literature [2.4].

Several samples with x between 1 and 0.7 were annealed in air at 400°C after a $CdCl_2$ treatment. Generally, the carrier density decreased to around 10^{14} /cm^3 for all the samples, showing only a weak concentration dependence. A typical mobility was around 2.0 cm^2/V-s. However, the ratio of the dark resistivity to the resistivity under AM1.5 conditions showed an increase after the annealing process, in some cases by a factor of 100. Some recent DLTS work by Lourenço,*et.al.*[2.5], with CdTe grown by CSS indicates that after an anneal with $CdCl_2$, more metastable minority carrier trap energies are formed while retaining the majority carrier trap associated with the CdTe. They conclude that annealing tends to improve the activation of the dopants due to removal of defects. The improved dark-to-light ratio in our alloys is consistent with this interpretation.

Persistent photoconductivity--CdS and in CdS_xTe_{1-x} alloys have shown evidence of persistent photoconductivity (PPC). We have made some measurements on the alloys in an effort to gather more information about the defect states that are responsible for the slow recombination of carriers after exposure to light. These defect states are usually attributed to

deep bistable states, strains, or macroscopic barriers introduced at barriers. In the past PPC has been modeled using a stretched exponential, but a more recent study by Hirsch, *et, al.*,[2.6] suggests that a gaussian distribution of capture barriers with a decay constant that depends on the capture barrier energy in an activated manner might also describe the decay.

Deng [2.7] has PPC data for the laser-grown alloys after exposure to AM1.5 radiation for x = 1 and x = 0.99. If a stretched exponential model is used, the decay constant τ is of the order of 10^6 minutes for the as-grown films and decreases to around 10 minutes for films annealed with $CdCl_2$. We have recently collected more extensive data for x = 0.99 and used the gaussian model to describe the PPC after a 5 minute AM1.5 exposure (see Fig. 2-4). Here the decay constant depends on the capture barrier energy and is given by: $\tau_d = \tau_0 \exp(E_c/kT)$. For both the as-grown and the annealed films the gaussian is typically centered at an energy of around 0.25 eV with a width of about 0.07 eV. However, τ_0 changes from about 0.1 seconds for the as-grown films to about 0.004 seconds for the annealed films. This is consistent with the reduction of strain and/or the reduction of macroscopic barriers in the annealed films. It should also be noted that the annealed films typically are more resistive than the as-grown films for low x values in these laser-grown alloys.

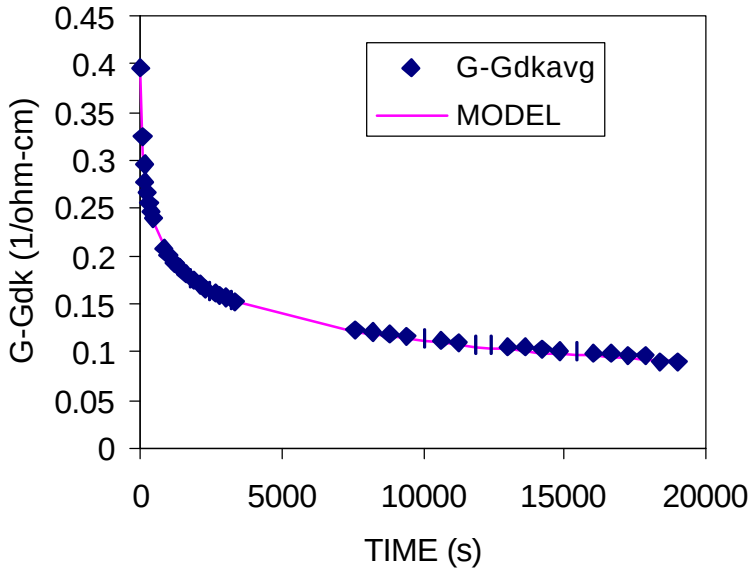

Fig. 2-4: PPC decay of the alloy film x = 0.99 after a 5 minute exposure to AM1.5 light at room temperature.

2.3 Optical absorption and the variation of energy gap with S content

We have supplied a complete set of the CdS_xTe_{1-x} alloy films to Dave Albin and Ramesh Dhere who have used a double beam optical spectrometer to study the transmission and reflection from

these films deposited on Corning 7059 glass. The films were very smooth with thicknesses typically in the range from 0.5 to 1.0 μm. Thus there are strong interference oscillations in transmission and reflection. Transmission and reflection signals were combined to yield the absorption coefficient. A summary of the data as analyzed by Dhere and Albin is shown in Fig. 2-5. This composite figure shows the absorption curves for the alloy films, the extrapolated values of band gap and a table showing the sample x-values and bandgap energies. Note that the films were very smooth and the data were not obtained with an integrating sphere. Transmission was corrected for reflection to remove the significant thin-film interference effects.

One of the interesting points in the analysis of the optical absorption is the interpretation of the fundamental band gap. Traditionally, people have used an extrapolation based on the joint density of states for optical transitions which has the form $\alpha \sim (h\nu - E_g)^{0.5}$. The quantum mechanical form also has the square of a matrix element for the transition. In some cases this is known to be linear in the momentum, k, of the photon--thus linear in photon energy. Thus the form would be

$$\alpha \sim h\nu(h\nu - E_g)^{0.5} \qquad (2.1)$$

Using this extrapolation, the band gaps are obtained as shown in Fig. 2-5. In our measurements on similar films, we have obtained essentially the same results. We have attempted to fit the band bending with a functional form quadratic in x, the sulfur concentration in the films. The fit is poor. Such behavior seems to be quite unusual for binary alloy films. It may be related to the existence of a structural phase transition near the middle of the alloy range. It may also be related to the fact that there is a large miscibility gap in this system.

2.4 Phonon Raman shifts vs. composition

Fig. 2-6 shows the longitudinal optical Raman frequencies for the full range of alloy films. For small x, the CdS-like LO_2 and TO_2 phonons converge to the triply-degenerate local vibrational mode of sulfur in CdTe at 259 cm^{-1}. Note that the LO_2, the CdS-like mode, exhibits a smooth, monotonic variation across the alloy range and increases substantially with sulfur concentration. This permits its use as a probe of the alloy composition. For example, it is possible to probe with laser excitation through the glass into the CdS and into the CdS_xTe_{1-x} alloyed region of a solar cell.

The lines represent the calculated results of the modified random element iso-displacement (MREI) model. Details of the MREI model and the fit to these data can be found in Ref. 2.2. The MREI model fits well except that the data appear to be systematically higher between x=0.2 and x=0.7. The Raman lineshapes indicate that there is substantial alloy broadening of the Raman peaks between x=0.1 and x=0.9. This effectively lowers the frequency of the observed Raman peak by 3 to 4 cm^{-1} from the phonon frequency at the Brillouin zone center.

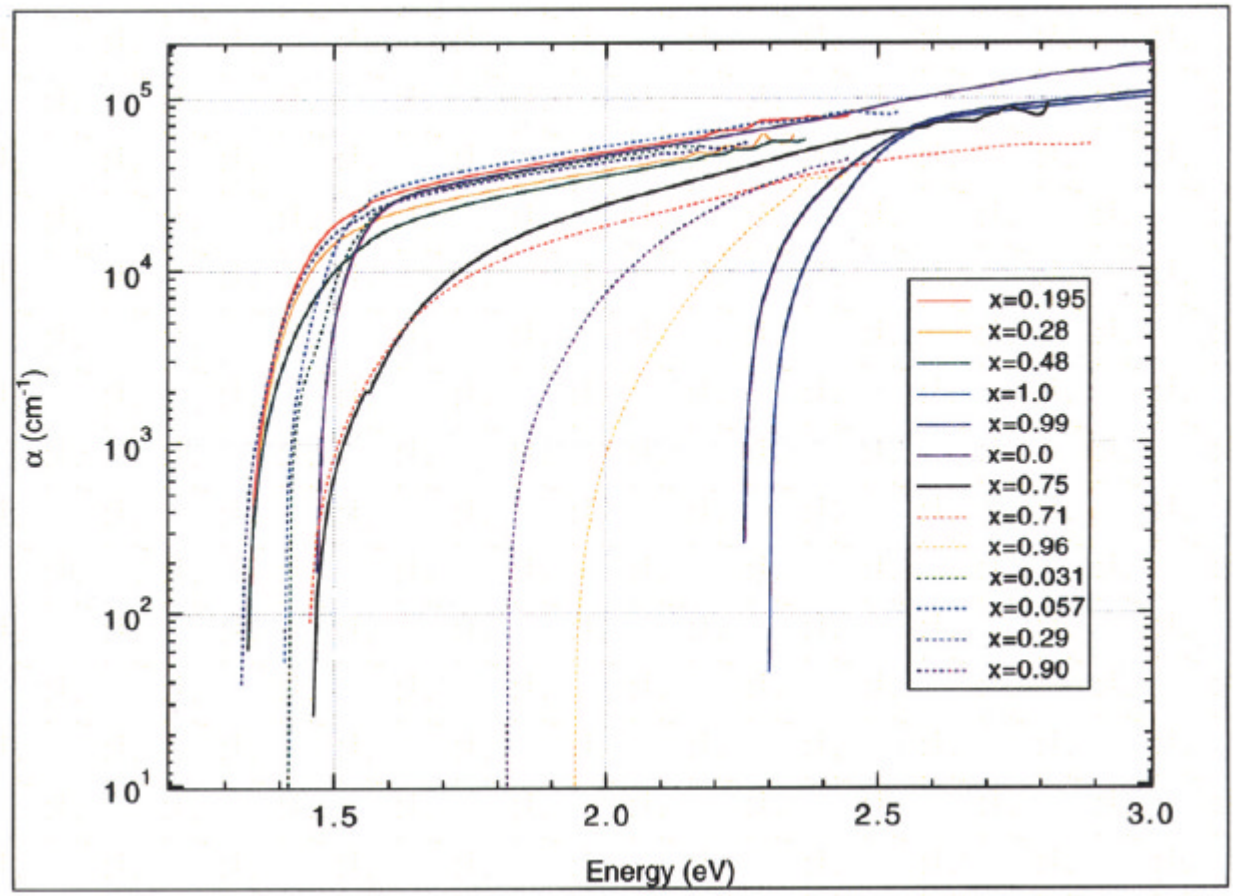

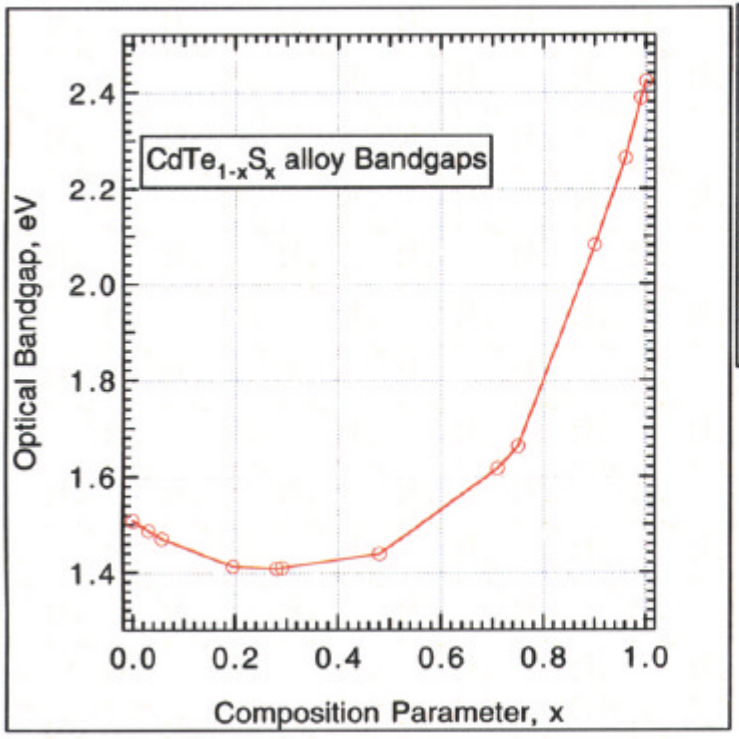

Optical Bandgaps Data for $CdTe_{1-x}S_x$ Alloy System (9/9/97)

Films Supplied by A. Compaan (U. of Toledo) made by Pulsed Laser Evaporation

Absorption Coefs and Bandgaps determined by D. Albin,R. Dhere (NREL) using Specular R,T measurements

Compositions determined by EPMA A. Mason (NREL)

Point	composition	bandgap
0	0	1.51
1	0.031	1.488
2	0.057	1.472
3	0.195	1.414
4	0.28	1.409
5	0.29	1.411
6	0.48	1.44
7	0.71	1.618
8	0.75	1.663
9	0.9	2.082
10	0.96	2.264
11	0.99	2.389
12	1	2.424

Fig. 2-5: Summary of the data by Dhere and Albin

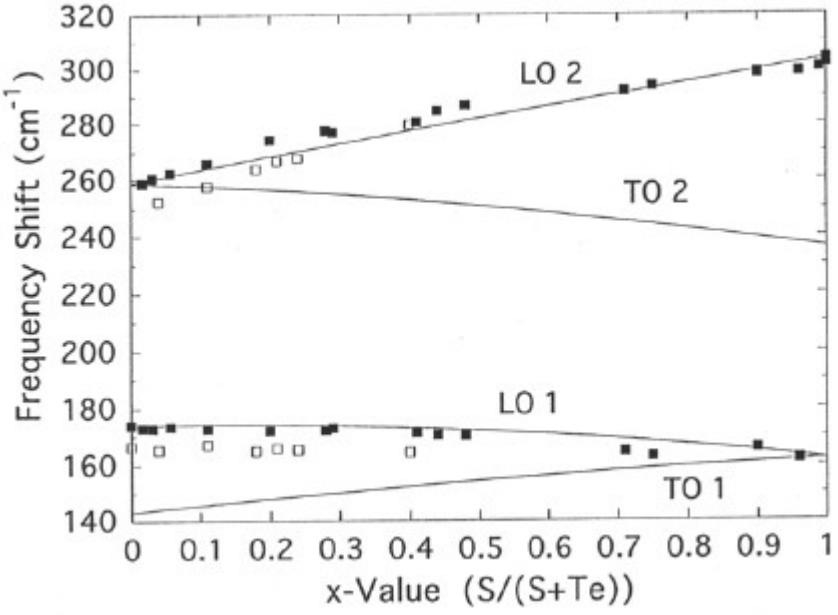

Fig. 2-6: Frequencies of the CdS-like and the CdTe-like phonon modes in CdS_xTe_{1-x}.

2.5 Short range clustering and Raman linewidths in the CdS_xTe_{1-x} alloy

The following discussion is excerpted from our paper on this subject that appeared recently in Applied Physics Letters.

The line shape of the first-order Brillouin-zone-center optical phonons of the CdS-like mode show an asymmetric broadening which arises from the restriction of the phonon to a finite volume and a shortening of the phonon coherence length.[2.8,2.9]

The phonon coherence lengths of the LO phonons can be determined from the line shape of the first-order Raman peaks using a one-dimensional linear chain model and following the spatial correlation model of Parayanthal and Pollak [2.9] In this model the Raman intensity I(ω) at a frequency ω can be expressed as:

$$I(w) \propto \int_0^1 \exp\left(-\frac{k^2 L^2}{4a^2}\right) \frac{d^3 k}{[w - w(k)]^2 + [\frac{\Gamma_o}{2}]^2} \qquad (2.2)$$

where k is the reduced wavevector (normalized to the Brillouin zone boundary value), a is the lattice constant and L is the phonon coherence length. For the LO phonon frequency dispersion the linear-chain model has been used.[2.10]

$$w^2(k) = A(x) + \sqrt{A^2(x) - B(x)[1 - \cos(pk)]}\,. \qquad (2.3)$$

To our knowledge, data for A(x) and B(x) are only available for the endpoints of the CdS_xTe_{1-x} system.[2.11] Thus, in our fits, we have set $A(x) = \frac{1}{2}\omega_o^2(x)$, where $\omega_o(x) = \omega(x,k=0)$ is the phonon frequency at the zone center. ω_o is adjusted until the peak location of the fitted lineshape according to Equation 2.2 coincides with the measured Raman peak. The parameter B(x), which determines the curvature of the CdS-like LO phonon dispersion curve, has been chosen such that $\omega(x,k=1)$, the phonon frequency at the zone boundary, equals $2^{-1/2}\ \omega_o(x)$. For example, we used $B(0.017)=57.12\times10^7$ cm^{-4} or $B(0.71)=96.60\times10^7$ cm^{-4} for the x=0.017 or x=0.71 alloy, respectively. This is consistent with pure CdS[2.11,2.12] with $B(1)=109.59\times10^7$ cm^{-4}.

The lattice dynamics calculations of Nusimovici and Birman [2.12] show the close correspondence between the Γ_5 (L) mode of the CdS hexagonal (wurtzite) structure and the LO_1 mode of the CdS cubic (sphalerite) structure. When the Brillouin Zone is unfolded along the hexagonal [0001] direction, the phonon modes are shown to be nearly identical to those of the cubic [111]. In particular, the curvature at Γ is nearly identical. Thus, we expect our analysis of lineshapes to be insensitive to the structural phase change from hexagonal to cubic which occurs near x = 0.4 in these films, which happen to be strongly oriented [0001] or [111].[2.13]

In addition to the detailed lineshape, we compared $\omega_o(x)$ with $\omega_{max}(x)$, the observed Raman peak position. The difference between the two quantities is caused by the breakdown of the k = 0 selection rule which causes the mean position of the Raman signal to shift to lower energy. Table 2.2 lists both quantities for the range of alloy compositions.

Table 2.2: Comparison of $\omega_o(x)$, and $\omega_{max}(x)$.

x-value	$\omega_o(x)$, [cm^{-1}]	$\omega_{max}(x)$, [cm^{-1}]
0.017	260	258.7
0.031	263	260.6
0.057	264	260.8
0.11	271.5	267.8
0.41	285.5	280.4
0.48	290	285.8
0.71	296.5	291.6
0.90	301	298.0
0.96	304.5	300.6
0.9922	305.5	302.7
1, (film)	306	303.6
1, (crystal)	305.6	305.6

For simplicity in solving Equation 2.2, we assumed a spherically symmetric shape of the phonon dispersion near the zone center so that $d^3k=4\pi k^2dk$. An example of a 10 K CdS-like

phonon Raman line and the corresponding line shape fit is displayed in Fig. 2-7 for the $CdS_{0.71}Te_{0.29}$ alloy. For the CdS spectrum (x=1) a natural linewidth of $\Gamma_o = 3\ cm^{-1}$ has been determined in our own measurement of single crystal CdS and used for all alloys. All data have been corrected for instrumental resolution.

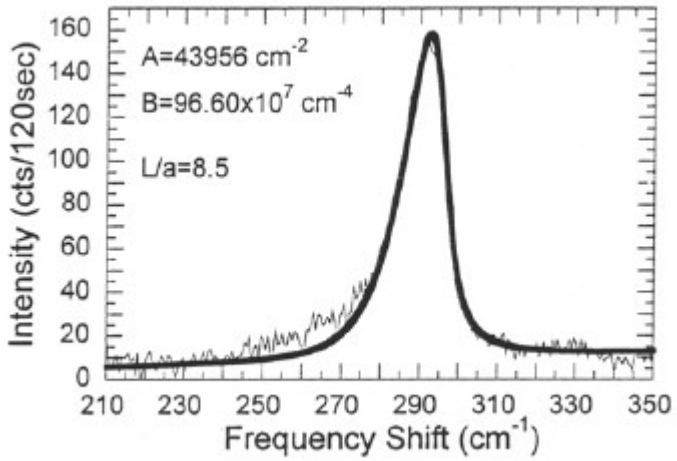

Fig. 2-7: 10 K CdS-like LO Raman signal of the $CdS_{0.71}Te_{0.29}$ alloy (thin line) and curve fit according to reference 2.9 (heavy line). The position of the peak maximum is $\omega_{max}(x=0.71) = 291.6 \pm 3\ cm^{-1}$, with the phonon frequency at the zone center of $\omega_o(x=0.71) = 296.5\ cm^{-1}$.

The CdS-like LO Raman peaks appear almost symmetric for alloys close to the endpoints of the CdS_xTe_{1-x} system and from the line shape fits coherence lengths of up to 15 lattice constants (~100 Å) have been determined. For single crystal CdS no asymmetry was found, as expected, corresponding to a coherence length of at least 50 lattice constants (detection limit of any asymmetry). Raman peaks of alloy compositions within the miscibility gap show a strong asymmetry with coherence lengths as small as 7.5 lattice constants (~45 Å) for the x=0.41 alloy. A summary of the entire set of coherence lengths is shown as square markers in Fig. 2-8.

The CdS_xTe_{1-x} system shows a large miscibility gap spanning the range between $0.16 \le x \le 0.86$ at a temperature of T=650°C.[2.14,2.15] The miscibility gap near 400°C is wider and extends from x=0.059 to x=0.97.[2.16,2.17] Single-phase films that exist within this gap are not in thermodynamic equilibrium, and hence, one should expect a large driving force for decomposition or phase separation in the material. Thus, for freshly grown alloys, we might expect the formation of local clusters of CdS or CdTe material in this nonequilibrium state, leading to finite coherence lengths and the asymmetric broadening of the LO phonon peaks explained by Eq. 2.2.

The chain length of a cluster is defined by a sequence of adjacent like anions in the S,Te sublattice. We model the dependence of the cluster size on the film composition and include a clustering probability by using the first-nearest neighbor Warren-Cowley [2.18] short-range order parameter α. The order parameter α is defined as $\alpha=(P(S|S)-x)/(1-x)$, where P(S|S) is the probability, given that a particular anion site is occupied by S, that its first-nearest neighbor anion site is also occupied by an S atom. Hence, α is zero if no clustering occurs at all (random distribution of S and Te), and equals one for a completely phase-separated material. We expect that the anions in alloys near the end points of the compositional range i.e., CdTe with trace

amounts of S (x≈0) and CdS with trace amounts of Te (x≈1), will be arranged in random fashion and that alloys at the midrange of the miscibility gap will undergo incipient phase separation (clustering) to the greatest extent. We assume that α is an analytic function of x which goes to zero at x=0 and x=1 and is at a maximum at x=0.5. The lowest order polynomial in x that has these properties is of the following (parabolic) form:

$$\alpha(x) = 4\,\alpha_{1/2}\,x\,(1-x) \tag{2.4}$$

where $\alpha_{1/2}$ is a fitting parameter equal to the Warren-Cowley short-range order parameter at x=1/2.

By considering a linear chain of atoms, the average chain length of like atoms on the anion sublattice has been calculated. Thus, the probability of finding a chain of n sulfur atoms in adjacent anion sites, suitably normalized, is:

$$P_S\,(x,n) = (x + (1-x)\,\alpha(x))^{n-1}\,(1-x)\,(1-\alpha(x)) \tag{2.5}$$

and similarly, for a chain of n adjacent Te anions, one obtains:

$$P_{Te}\,(x,n) = ((1-x) + \alpha(x)\,x)^{n-1}\,x\,(1-\alpha(x)) \tag{2.6}$$

where n is an integer. The average chain length of S anions, L_S, or Te anions, L_{Te}, therefore becomes:

$$L_i\,(x) = \sum_{n=1}^{M} n\,P_i\,(x,n) \;/\; \sum_{n=1}^{M} P_i\,(x,n) \tag{2.7}$$

with i representing either S or Te.

The upper limit of the chain length M is determined by a finite grain size of the films studied. From SEM micrographs we determined grain diameters d of roughly 800 Å, independent of the composition of the alloy, therefore we set $M=d/(a\sqrt{3})\approx 80$ for the entire set of samples (lattice constant a=6.3 Å for the zincblende structure of CdTe). We found that L(x) is not too sensitive to M, a variation by ±10 did not make a noticeable difference to the fit. For the average length L(x) of a cluster we obtain:

$$L(x) = [L_S(x) + L_{Te}(x)]/2 \tag{2.8}$$

Besides the phonon coherence lengths obtained from the lineshape fits (see Fig. 2-7), Fig. 2-8 also contains the calculated average cluster size according to Equation 2.8 (solid curves). The function L(x) for the cluster size fits the observed coherence lengths (square markers) within the experimental error for $\alpha_{1/2} = 0.73$. Note that $\alpha_{1/2}$ is the only adjustable parameter in the calculated coherence length, L(x). Although the function L(x) is not strongly dependent on M, it is sensitive to a variation of less than 0.01 in the $\alpha_{1/2}$ parameter which is our estimated error for this quantity. In Fig. 2-8 the lower curve shows the cluster length, L(x) for $\alpha_{1/2}=0$ (no clustering). This curve is roughly equivalent to the Raman linewidth data given by Bergman, *et al*.[2.19] for

the alloy system $Al_xGa_{1-x}N$ which does not have a miscibility gap, and apparently has no tendency to cluster.

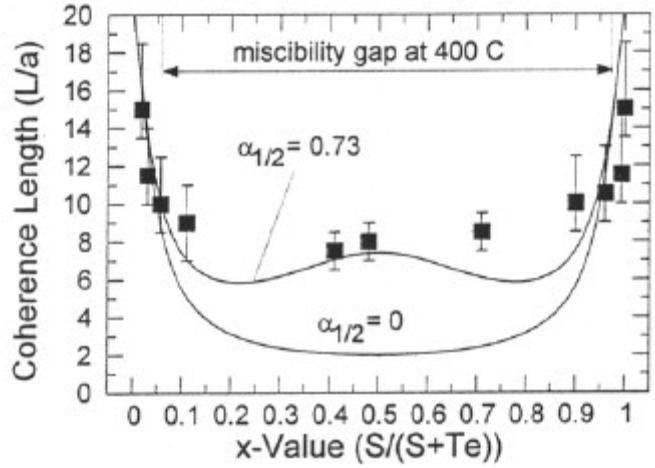

Fig. 2-8: CdS-like LO phonon coherence lengths determined according to Eq. 2.2 (filled squares). The average cluster size, calculated from Eq 2.8, is shown for two cases, with the Warren-Cowley short-range order parameter $\alpha_{1/2} = 0.73 \pm 0.01$ and $\alpha_{1/2} = 0$.

In summary, for the CdS_xTe_{1-x} alloy system our line shape study of LO Raman lines of the CdS-like LO phonons has shown a composition dependence of the phonon coherence lengths. Alloys with compositions well within the miscibility gap have coherence lengths down to 7.5 lattice constants whereas films with x grown outside this gap show coherence lengths of up to 15 lattice constants. $\omega_o(x)$, the phonon frequency at the zone center, has been inferred for each alloy and found to be up to 5.1 cm^{-1} higher than $\omega_{max}(x)$, the observed Raman peak position, for the alloy with x=0.41.

With a simple probability argument using an x-dependent Warren-Cowley short-range order parameter, a composition-dependent average cluster length has been calculated which agrees with the observed phonon coherence lengths. Thus we have shown how the Raman lineshape and asymmetry resulting from phonon confinement or spatial correlation effects can yield a short-range order parameter (microclustering probability). This short-range ordering is strong in the case of the CdS_xTe_{1-x} alloy system with its large miscibility gap.

References

2.1 "Properties of CdS_xTe_{1-x} Alloy Films", A. Fischer, X. Deng, D. Grecu, K. Makhratchev, X. Ma, R. Wendt, D. Zuo, A.D. Compaan, and R.G. Bohn, *Proc. 26th IEEE Photovoltaic Spec. Conf.*, Anaheim, CA, 447-450 (1997)

2.2 A. Fischer, Z. Feng, E. Bykov, G. Contreras-Puente, A. Compaan, F. de Lande, J. Avendano, and Alice Mason, Appl. Phys. Lett. **70**(24), (1997), pp. 3239-3241

2.3 J.W. Orton, B.J. Goldsmith, M.J. Powell, and J.A. Chapman, Appl. Phys. Letts. **37** (1980), p. 557

2.4 L.C. Isett, J. Appl. Phys. **56**, 1984, p. 3508

2.5 M.A. Lourenço, Yip Kum Yew, K.P. Homewood, K. Durose, H. Richter, and D Bonnet, J. Appl. Phys. **82**(3), 1997, p. 1423

2.6 Michele T. Hirsch, J.A. Wolk, W. Walukiewicz, and E.E. Haller, Appl. Phys. Lett. **71**, 1098 (1997)

2.7 X. Deng, M.S. Thesis, The University of Toledo (unpublished)

2.8 H. Richter, Z.P. Wang, and L. Ley, Solid State Commun. **39**, 625 (1981).

2.9 P. Parayanthal and F.H. Pollak, Phys. Rev. Lett. **52** (20), 1822 (1984).

2.10 C. Kittel, *Introduction to Solid State Physics* (Wiley, New York, 1967), 3rd ed., Chap. 5.

2.11 H. Bilz and W. Kress, *Phonon Dispersion Relations in Semiconductors*, (Springer-Verlag, Berlin, 1979) pp.113 & 120.

2.12 M.A. Nusimovici & J.L. Birman, Phys. Rev. **156**, 925 (1967).

2.13 A. Fischer, X. Deng, D. Grecu, K. Makhratchev, X. Ma, R. Wendt, D. Zuo, A.D. Compaan, and R.G. Bohn, in *Proc. 26th IEEE Photovoltaic Specialists Conference—1997*, (IEEE, Piscataway, N.J., 1997) p. 447

2.14 K. Ohata, J. Saraie, and T. Tanaka, Jpn. J. Appl. Phys. **12**, 1198 (1973).

2.15 S.Y. Nunoue, T. Hemmi, and E. Kato, J. Electrochem. Soc. **137**, 1248 (1990).

2.16 M.E. Özsan, D.R. Johnson, D.W. Lane, and K.D. Rogers, *12th Euro. Phot. Sol. Energy Conf.*, (Amsterdam, 1994) p. 1600.

2.17 G.D. Jensen, B.E. McCandless, and R.W. Birkmire, Mat. Res. Soc. Symp. Proc. **426**, 325 (1996).

2.18 J.M. Cowley, J. Appl. Phys. **21**, 24 (1950); F. Ducastle, *Order and Phase Stability in Alloys*, (North-Holland, Amsterdam, 1991) p.51.

2.19 L. Bergman, M.D. Bremser, W.G. Perry, R.F. Davis, M. Dutta, and R.J. Nemanich, Appl. Phys. Lett. **71**, 2157 (1997).

3.0 Studies of CdS/CdTe interdiffusion

3.1 Grazing incidence x-ray measurements with Buffalo/Brookhaven collaborators

In last year's annual report, we presented data from grazing incidence x-ray scattering (GIXS) which provides information on interface roughness. In this report, we shall highlight studies of angular dependence of x-ray fluorescence (ADXRF) on samples which have been subjected to various $CdCl_2$ anneals. The ADXRF provides information on interdiffusion of Te into CdS provided the layers are thin enough.

Heterojunction samples used in the present experiment were prepared by rf planar magnetron sputtering. The film deposition conditions were the same as reported in Ref. 3.1 which has yielded cells with 11.6% efficiency for one-sun illumination. The typical CdTe cell has a superstrate structure with soda-lime glass/SnO_2:F/CdS/CdTe/metal. We call this ordering of the semiconductors the "normal" structure. For our cells, the CdS and CdTe thicknesses are typically 0.1 to 0.2 μm and 2 to 4 μm, respectively. For the ADXRF work, very thin films (bilayers of CdS and CdTe) were sputtered directly onto Corning 7059 glass to take advantage of the smoother surface. A "normal" (CdTe on CdS on BSG glass) and an "inverted" (CdS on CdTe on BSG) bilayer heterojunction were investigated for comparisons. The nominal layer thickness for CdTe and CdS layers in these samples was approximately 20 ± 5 nm. Four samples were prepared and annealed in our vapor $CdCl_2$ annealing system for 30 min at temperatures of 340, 355, 370, and 387 °C.

In essence, the ADXRF technique is based on the complex refractive index $n=1-\delta-i\beta$ of the material under study at x-ray wavelengths. Both δ and β contain element-specific information depending on the mass density; the characteristic photoabsorption cross-sections for different elements are usually well separated in energy. At a low incidence angle, x-ray scattering and fluorescence signals are sensitive to structural/compositional discontinuities (or interfaces) in the layer structure. Through a control of the x-ray probing depth and field distribution by varying the wavelength and incidence angle, the ADXRF measurements allow a *nondestructive* method to obtain important microstructural information about the interfaces, such as the layer thickness and depth profile of specific atomic species in the material. X-ray fluorescence and anomalous scattering are particularly useful as an *element-specific* method for probing the impurity accumulation and intermixing of constituent atoms in the interfacial region. Theoretical analysis of x-ray propagation in layer structures as well as methods used for obtaining interfacial roughness and correlation lengths can be found in References 3.2 and 3.3.

In the treatment of x-ray fluorescence yield (FY) we neglect the incoherent scattering contributions and assume that x-ray photons lose all energy via excitation of the atoms in the material to different states. The small energy losses to Compton effect, phonon scattering, etc. are all neglected. Thus, the FY intensity is proportional to the energy absorbed in the layers as well as the density profile of fluorescent atoms, and it can be written as [3.3,3.4]:

$$I_{FY} \propto \int_{D} d\,z \left(-\frac{d\,S_z}{d\,z} \right) \rho_{FA}(z), \qquad (3.1)$$

where S_z is the z-component (perpendicular to the interfaces) of the Poynting vector, $\rho_{FA}(z)$ is the density profile of the fluorescent atoms in the z-direction, and D is the x-ray penetration depth. In an ADXRF experiment, the x-ray penetration depth is changed by varying the incidence angle, the results can provide useful information about the compositional depth profile normal to the surface pertaining to a selected atomic species in the layer material.

The x-ray fluorescence output for a given field distribution at a fixed incidence angle can offer information on the concentration depth profile of atoms which produce the fluorescence yield (see Eq. 3.1). By varying the probing depth of x-rays through changes of the incidence angle, relative variations in the content of a specific atomic species around the interface can therefore be compared. Using this ADXRF technique, we have investigated the effect of thermal annealing on the inverted junction bilayer films.

To provide a simple picture of the overall angular variation of Te fluorescence yield for this inverted junction, the x-ray flux distribution inside the sample for various incidence angles was calculated first. At a given incidence angle, the spatial variation of the field intensity is thus obtained, and the characteristic length of intensity decay in the material is determined as the penetration depth for that particular incidence angle [3.3,3.5]. For a given penetration depth of the x-ray beam (corresponding to a specific incidence angle), the total intensity of x-ray fluorescence yield can be obtained by integration in accordance with Eq. 3.1. The calculated photon flux spatial distribution in sample UB-2 is shown in Fig. 3-1 for various grazing incidence angles θ below (θ = 0.03° and 0.05°), above (θ = 0.1°), and at the critical angle (θ_c = 0.075°) at 31.9 keV, the energy used in our ADXRF measurements. In this calculation, structural parameters obtained earlier from our specular reflectivity data were used and the value of critical angle was determined self-consistently by using this procedure. The oscillations of flux distribution are caused by interference between the transmitted and reflected x-ray fields inside the layered material.

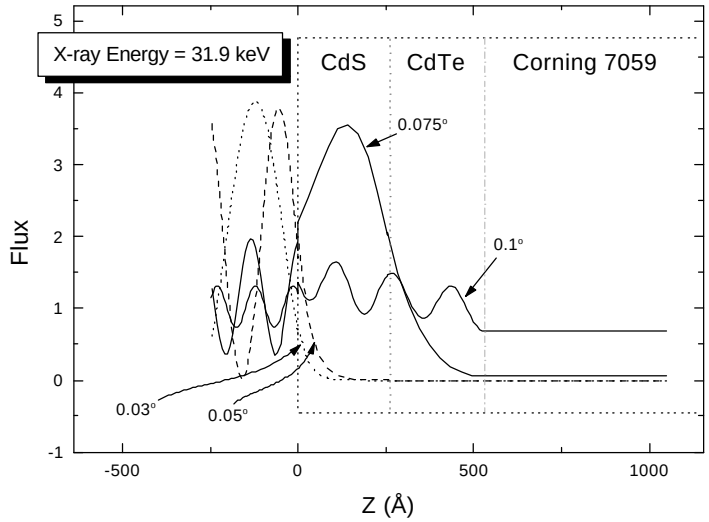

Fig. 3-1: Calculated depth distribution of x-ray flux in sample UB-2 for various incidence angles.

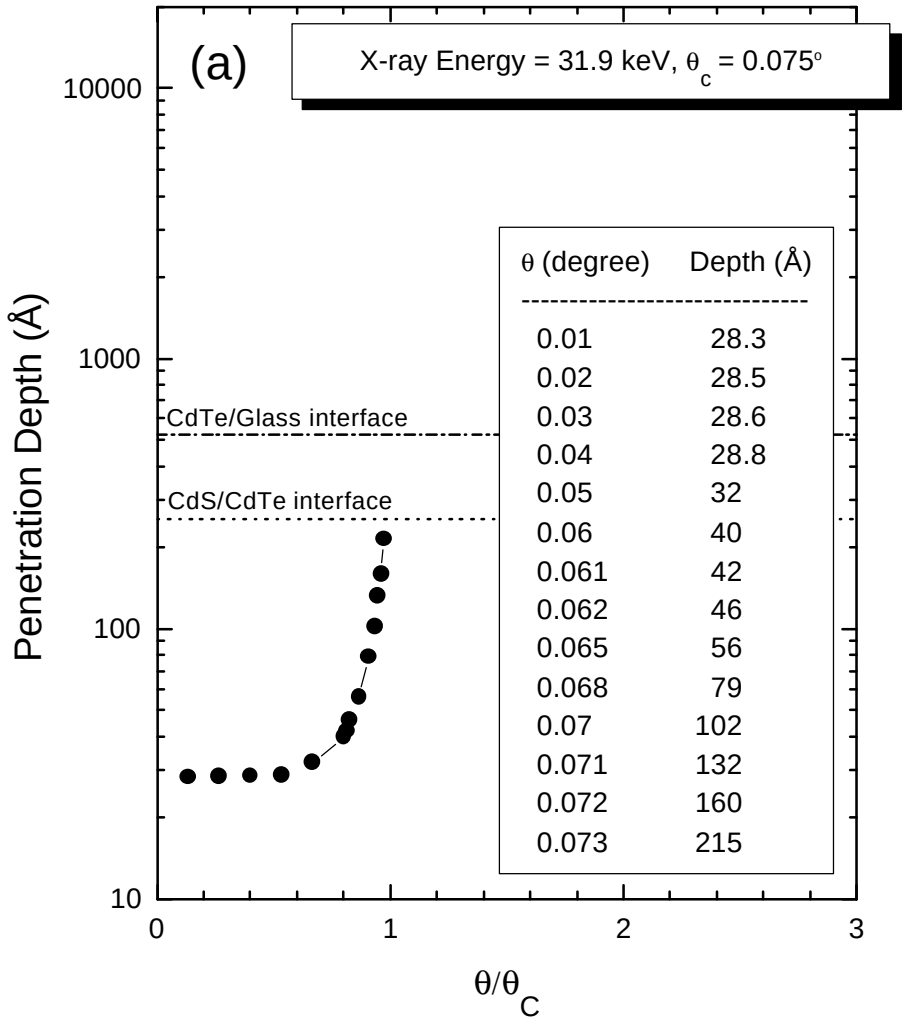

Fig. 3.2: Calculated penetration depth of x-ray beam vs. incidence angle for sample UB-2.

Based on the flux distribution shown in Fig. 3.1, the penetration depth of x-rays in this heterojunction as a function of the incidence angle is shown in Fig. 3.2. This plot can be used to convert the incidence angle to the corresponding x-ray penetration depth for investigating the depth profile of Te atoms around the interface.

The ADXRF measurements were performed at beamline X3B1 at National Synchrotron Light Source at Brookhaven National Laboratory, some experimental details have been reported recently [3.6]. Incident photon energy of 31.9 keV was selected by using a Si(111) double-crystal monochromator. A two-axis goniometer with angular resolution of 0.001° was used to rotate the

sample and thus control the grazing incidence angle θ between the incident x-ray beam and the film surface. For a precise sample alignment, a selected angle say θ = 0.07° was first determined accurately from specular reflectivity measurements with an Ar-flowing ionization chamber, and this angle was then used as a reference for defining other incidence angles. The x-ray fluorescence photons from irradiated samples were collected using a solid state Si(Li) detector calibrated with an energy resolution of 175 eV at the energy of Mn Kα emission (5.899 keV). The x-ray fluorescence spectra were obtained by using a multichannel pulse-height analyzer and the intensities of Cd Kα at 23.174 keV and Te Kα at 27.472 keV were obtained by curve-fitting the spectra with Gaussian peaks and a constant background. The Cd Kα and Te Kα fluorescence intensities are all normalized to the Cd Kα intensity at θ = 0.2° for each sample. The ADXRF results are shown in Figs. 3-3 and 3-4.

From Fig.3-3 it can be seen that at low incidence angles (below 0.07°) the Cd Kα FY intensity for the annealed samples increases more rapidly than the unannealed sample. At low angles (below the critical angle) as the incident x-ray penetrates deeper (increasing z) into the material with increasing θ, a higher rate of FY intensity corresponds to a higher concentration of the fluorescent atoms (see Eq.3.1) present near the sample surface. Hence, there are more Cd atoms present near the surface after annealing. It perhaps should be noted that changes in the Cd depth profile are similar for samples annealed between 340°C and 370°C, but a large change was found with a sample annealed at 387°C. In this analysis, we have taken into account possible changes in the angular dependence of Cd FY due to different thickness values of the CdS and CdTe layers which were determined accurately from our measurements of grazing incidence x-ray scattering [3.6]. The large variation between samples annealed at 370°C and 387°C cannot be attributed to the size effect.

The results of Te FY are shown in Fig. 3-4. In comparison with the increase in Cd FY intensity at low incident angles shown in Fig. 3-3, the angular dependence of Te FY increases more rapidly with increasing annealing temperature than Cd. This indicates that there is a stronger effect of Te migration from CdTe to CdS. We have also performed model calculations for changes of either CdS or CdTe layer thickness and also with Cd diffusion from CdTe to CdS; all these effects cannot account for the observed large changes in the angular dependence of Te FY. For a quantitative comparison, the intensity of Te Kα FY is divided by that of Cd Kα and plotted as a function of the incidence angle in Fig. 3-5 for all the five samples. At high incidence angles (above 0.1°) where the x-rays penetrate all the way through the sample, each of the ratio curves attains a more or less constant level, indicating an essentially constant concentration ratio of Te/Cd deep in the heterojunction. On the other hand, in the low angle region (below 0.05°) where the x-rays only penetrate to a shallow depth in the CdS layer, the Te/Cd FY ratio shows a strong dependence on the annealing temperature. Below 370°C, the Te/Cd ratio in this low angle region remains practically constant for a given annealing temperature except with some minor monotonic variations caused by edge effects. Noticeably, for the samples annealed at 370°C and 387°C, the Te/Cd ratio at low angles jumps to values even higher than the high-angle level.

Hence, Te and Cd migration in the inverted junctions (glass/CdTe/CdS) due to heating at 370°C or higher temperatures could result in a strong intermixing of the constituent atoms Te and Cd to the extent that the original window layer CdS can even behave somewhat like an absorbor with a high Te/Cd ratio. Direct comparison with similar ADXRF spectra obtained with normal junctions (consisting of glass/CdS/CdTe) also confirms this conclusion [3.6]. We believe that

although this analysis is based on an oversimplified model, the presence of a high Te/Cd ratio component in the CdS layer is clearly demonstrated in our experiment.

In conclusion, our ADXRF results show that a redistribution of both Cd and Te atoms has taken place in the inverted (glass/CdTe/CdS) heterojunctions after thermal annealing. The heat treatment tends to reduce the original Te concentration contrast between CdS and CdTe layers and results in a blurred interface. When the annealing temperature exceeds a certain critical value such as 370°C in our samples, an inverted junction can be transformed into a complicated admixture behaving like a normal junction near the surface of CdS, as manifested by a Te/Cd concentration ratio higher than that in the second (CdTe) layer. In a separate experiment we have found that the interfacial roughness at the CdS/CdTe interface also changes significantly with annealing temperature in these heterojunctions [3.6]. These results of *nondestructive* characterization of heterojunctions using ADXRF could therefore serve as useful tools for the control of atomic intermixing in the growth of thin film photovoltaic materials.

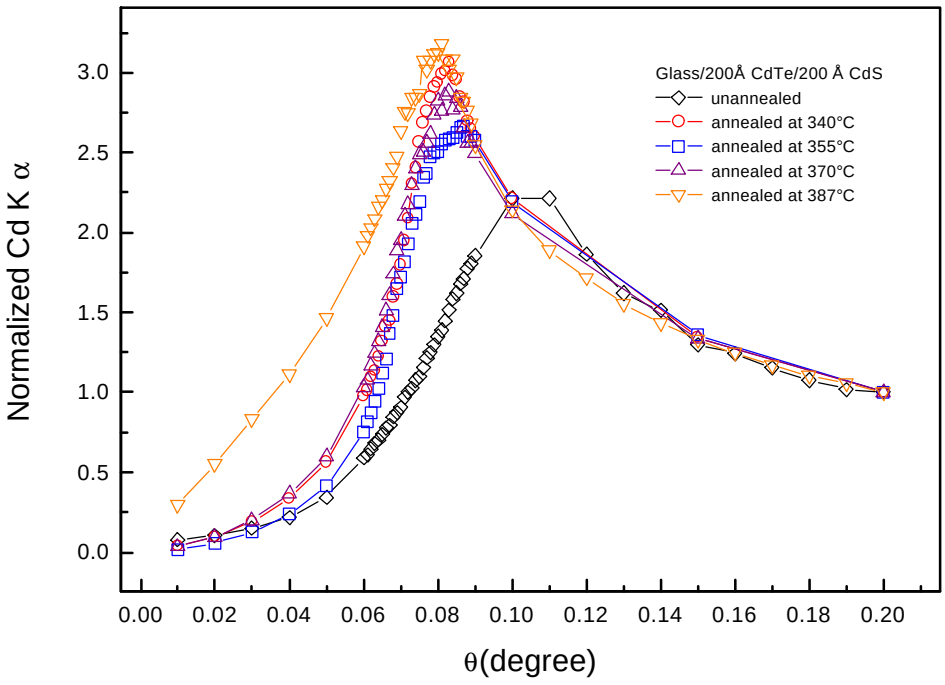

Fig. 3-3: Angular dependence of Cd Kα fluorescence intensity normalized to the value at 0.02°.

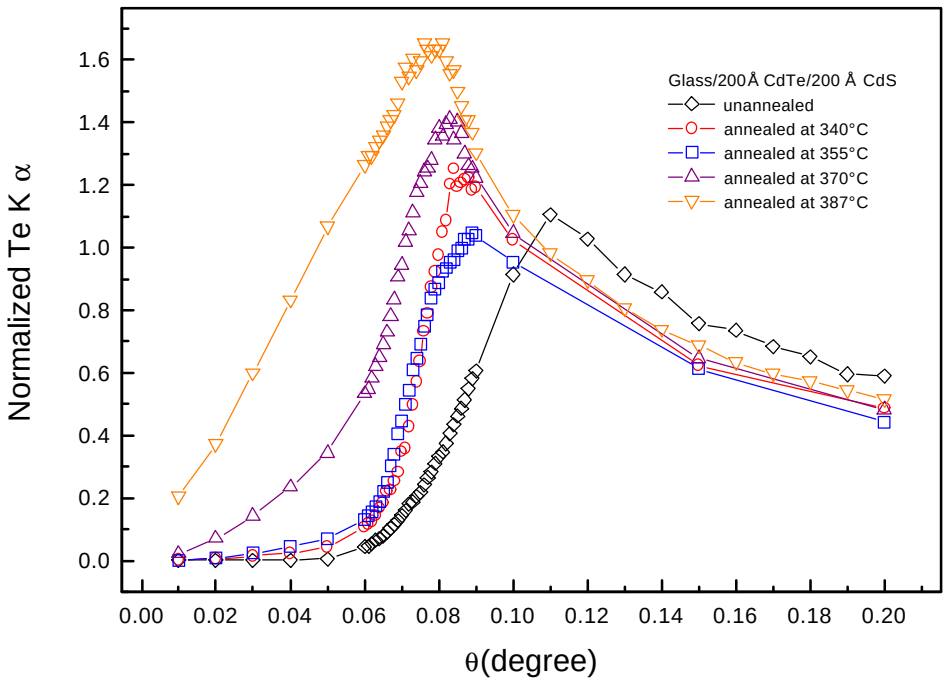

Fig. 3-4: Angular dependence of Te Kα fluorescence intensity normalized to the value at 0.02°

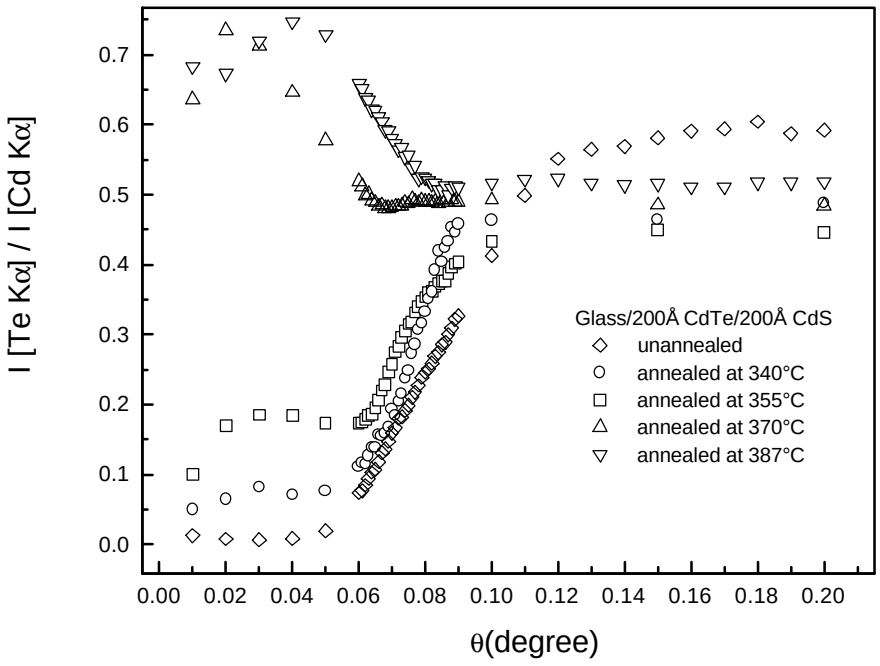

Fig. 3-5: Angular dependence of Cd Kα/Cd Kα FY in BSG/20nm CdTe/20 nm CdS bilayer.

3.2 XPS measurements of annealed BSG/CdS/CdTe structures

The grazing incidence x-ray fluorescence measurements described above imply that in the inverted bilayer structures S is diffusing through the CdTe layer above. X-ray photoelectron spectroscopy (XPS) provides another method to examine the surface conposition. In collaboration with Case Western Reserve University we have made XPS measurements on similar bilayer films with the inverted structure (BSG/CdTe/CdS). The spectra are shown in Fig. 3-6 below for anneal temperatures of 340, 360, 380 and 400°C. The Te $3d_{5/2}$ peak in tellurium oxide, probably TeO_2, is well separated from the equivalent peak in CdTe. The data indicate that at the higher temperature anneal treatments the CdTe signal is preferentially suppressed. This may result from growth of a thicker tellurium oxide layer but it may also result from coverage by other compounds. In fact, other XPS spectra indicate increased amounts of S in the surface layer. Some of this change may result simply from sublimation of outer CdTe layer, but the data are also consistent with out-diffusion of S from the underlying layer of the bilayer structure.

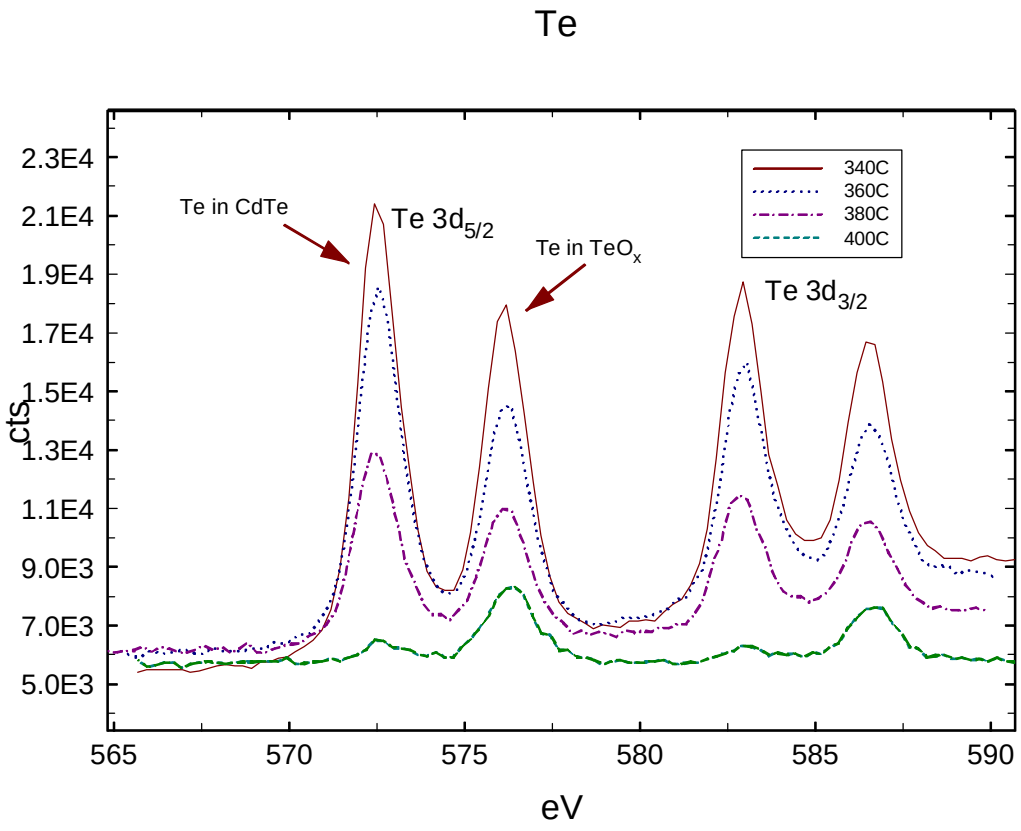

Fig. 3-6: Photoelectron spectra from bilayer films annealed in $CdCl_2$ vapor for 30 min. at four different temperatures.

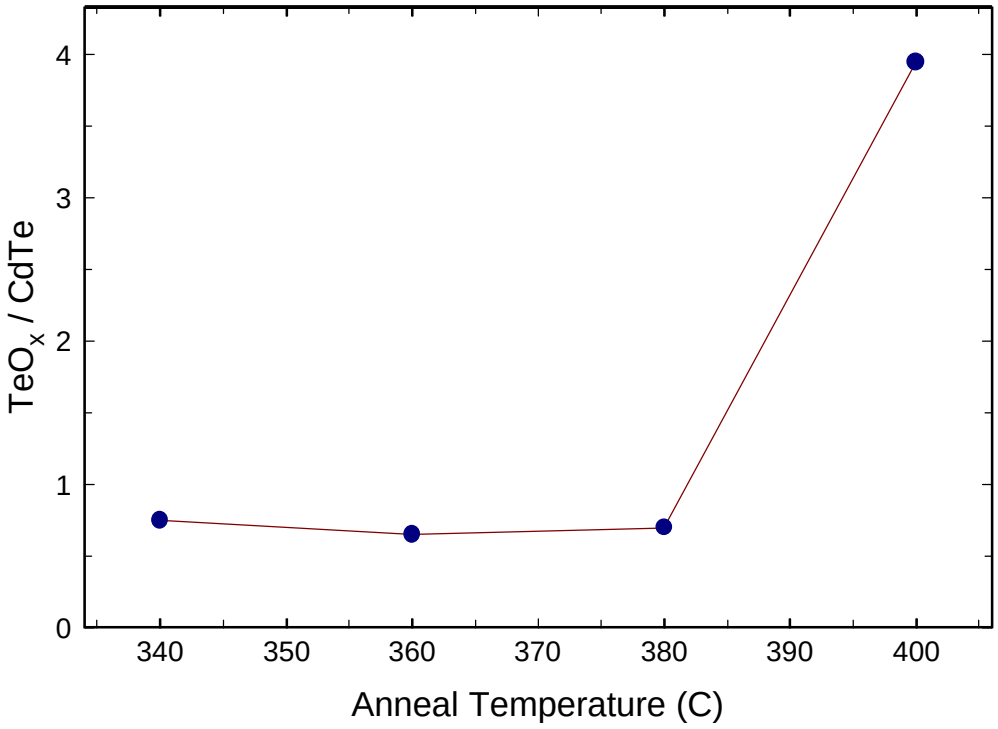

Fig. 3-7: Ratios of the Te $3d_{5/2}$ peaks near 575 eV for TeO_x and CdTe.

By plotting the ratio of TeO_x-related peak to the CdTe-related peak, we observe in Fig. 3-7, that the tellurium oxide is growing preferentially with respect to the CdTe mainly at temperatures above 380 °C.

3.3. Performance of sputtered cells vs. $CdCl_2$ treatment/anneal temperature

In order to check how these changes in the surface composition and the indications of S diffusion through the CdTe might be related to cell performance, we prepared solar cells with the same anneal procedures as for the bilayer films. Two differences should be noted: The first is that the solar cells semiconductor layers are prepared in the normal ordering rather than in the inverted ordering. The second is that the top layer (2.5 μm CdTe) is much thicker than the CdS top layer (0.02μm) in the inverted bilayer structures. The results for the cell performances are shown in the following three figures showing open circuit voltage (Fig. 3-8), short circuit current (Fig. 3-9), and cell efficiency (Fig. 3-10).

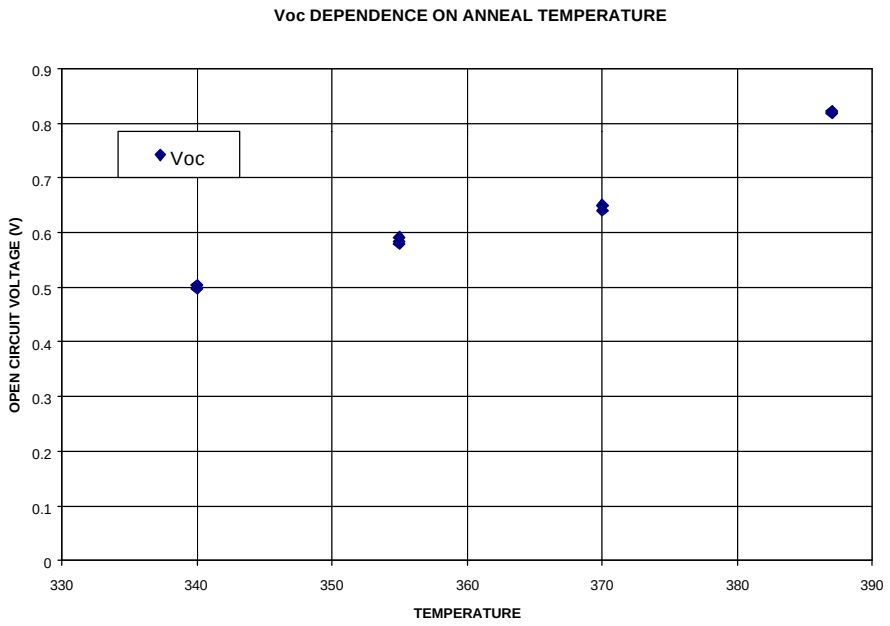

Fig. 3-8: V_{OC} of best three cells on films annealed similarly to the bilayer films.

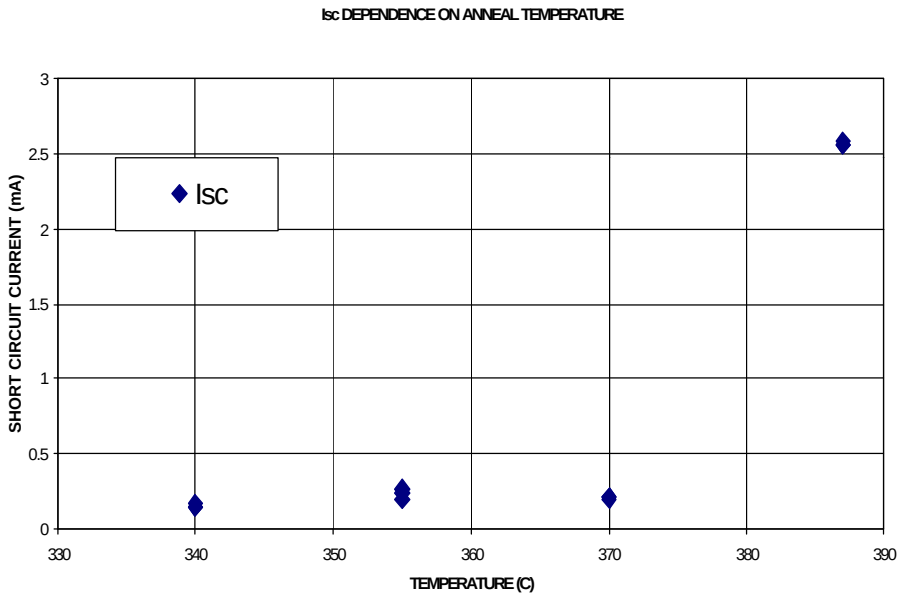

Fig. 3-9: I_{SC} of best three cells on films annealed similarly to the bilayer films.

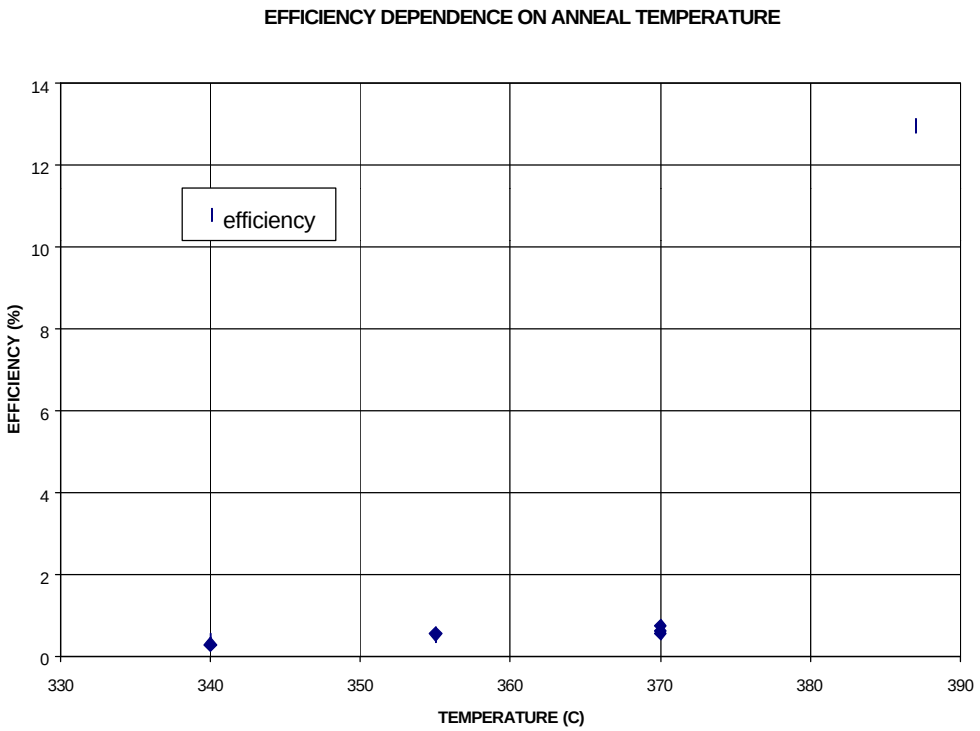

Fig. 3-10: Efficiency of best three cells on films annealed similarly to the bilayer films.

From these results it is clear that 380°C is a "critical temperature" with improved short-circuit current and efficiency for cells annealed above that temperature.

References

3.1 M. Shao, A. Fischer, D. Grecu, U. Jayamaha, E. Bykov, G. Contreras-Puente, R.G. Bohn, and A.D. Compaan, Appl. Phys. Lett. **69**, 3045 (1996)

3.2 Z.H. Ming, A. Krol, Y.L. Soo, Y.H. Kao, J.S. Park, and K.L. Wang, Phys. Rev. B **47**, 16373 (1993); and references cited therein

3.3 A. Krol, C. Sher, and Y.H. Kao, Phys. Rev. B **38**, 8579 (1988)

3.4 D.K.G. de Boer, Phys. Rev. B **44**, 498 (1991)

3.5 L.G. Parratt, Phys. Rev. **35**, 350 (1954)

3.6 Y.L. Soo, S. Huang, Y.H. Kao, and A.D. Compaan, J. Applied Phys. **83**, 4173 (1998)

4.0 Advances in rf sputter deposition

4.1 Implementation of a new vapor $CdCl_2$ treatment/annealing system

For CdTe-based solar cells, the $CdCl_2$ treatment process is a critical step in obtaining high performance, almost independent of the deposition process. For some time we have been using pulsed laser deposition (PLD) for the controllable application of a thin layer of $CdCl_2$. We found that PLD of a 0.1 to 0.2 μm layer produced much more uniform performance over a two-inch square area than the eye-dropper or dipping method with a $CdCl_2$-methanol solution. However, the PLD method is time consuming as it requires a vacuum deposition step and then a separate annealing step. Therefore, in this phase, we developed a vapor $CdCl_2$ treatment process following the method outlined by Brian McCandless of IEC [4.1]. The design and construction of the system was carried out as a senior thesis in the UT College of Engineering by Martin Hardin. Assistance on some of the construction and testing of the system was provided by graduate students Konstantin Makhratchev and Diana Shvydka.

The system is based on two SiC_6-coated graphite susceptor blocks (~3 inch square and 0.75 inch thick) with the lower susceptor milled out to provide a cavity for the $CdCl_2$. Our 2.75 inch by 3 inch substrates are placed face down over the cavity. The assembly is housed in a four-inch diameter quartz tube which is enclosed and fitted for evacuation and source gas flow. We have found best results with a gas flow of 5 sccm pulsed for one minute out of every 15 minutes during heating. We normally drive top and bottom susceptors to the same temperature. Heating is provided by linear, 800 W tungsten-halogen lamps and parabolic reflectors above and below the quartz tube. A charge of $CdCl_2$ consists of adding 1.5 ml of saturated $CdCl_2$ in methanol into a warm susceptor followed by conditioning of the charge at the normal gas flow and annealing temperature of 390 °C for 10 hours. During this conditioning, we employ a dummy substrate with a CdTe film. This process results in noticeable CdTe sublimation, some of which undoubtedly deposits in the lower susceptor cavity.

Fig. 4-1 shows a diagram of the vapor $CdCl_2$ treatment system. Although the best cells produced with this process are only marginally higher in performance than those produced

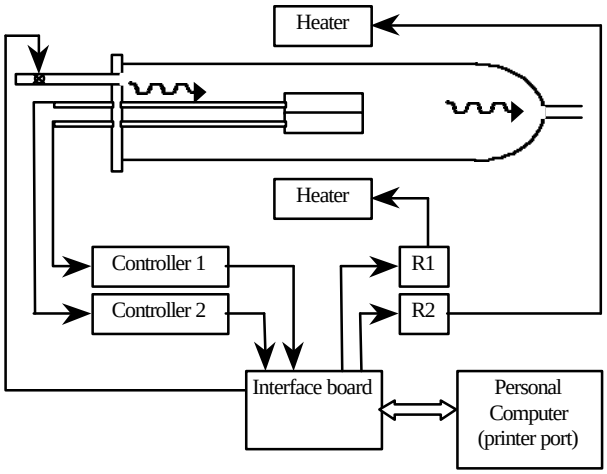

Fig. 4-1: Vapor $CdCl_2$ treatment system for three-inch substrates.

with the laser-deposition-followed-by-tube-furnace-annealing process, the uniformity and reproducibility is considerably better. This processing method also has the distinct advantage of not requiring a rinse in either deionized water or methanol. Thus our current cell fabrication has no wet chemical steps after the glass cleaning. Our current anneal process uses a 30 min. treatment at 387 °C.

4.2 Studies of combined rf/dc sputtering

During a brief, three-month postdoctoral visit to our lab in the period Mar.-May, 1997, Dr. Ralf Wendt completed a series of depositions and other measurements to examine the potential for the use of combined rf and dc excitation of the sputtering cathode during deposition of CdTe layers. This work was a natural extension of the Ph. D. work he had done at the Hahn Meitner Institute under the direction of Dr. Klaus Ellmer. Much of Dr. Wendt's study in our lab will be published in an article in the Journal of Applied Physics (scheduled for 9/1/98). An abbreviated description of this work is excerpted and summarized below:

In this study we examined how the plasma density affects CdTe film quality and solar cell performance. The CdTe films are characterized by *in situ* transmission measurements during the film growth, and by *ex situ* scanning electron microscopy (SEM) and photoluminescence. Results of the solar cell performance are presented in terms of open circuit voltage, short circuit current and fill factor. We adjust the plasma density by adding a dc component to the target self-bias potential. To vary the plasma density without changing the deposition rate we superpose an rf and a dc discharge and adjust the rf power to keep the deposition rate constant. A constant deposition rate is necessary to separate effects originating from the plasma density and those originating from the deposition rate. This method is based on recent work by one of the authors (RW) on ZnO films [4.2]. For TiN growth, Hultman, *et al*., [4.3] studied the effects of the plasma by using an additional external magnetic field to adjust the plasma density during sputtering.

Superposition of rf and dc discharges--Reviews of magnetron sputtering are given in [4.4] and [4.5]. Characteristic of this kind of discharge is the magnetic confinement of the plasma in front of the powered electrode which consists of the target material to be sputtered. The plasma density will depend on the magnetic field strength and geometry, and we have shown that an unbalanced magnetic field magnetron yields better solar cell performance than a balanced field magnetron. In general the confinement of the plasma is less for an unbalanced sputtering source than for a balanced one [4.6,4.7]. In the present experiments we used an unbalanced sputtering source but controlled the plasma density by the ratio of rf power to dc current to the magnetron. In general for the same deposition rate, rf sputtering is characterized by higher plasma density than dc sputtering [4.2]. When dc and rf are combined to drive the powered electrode, the plasma density can be adjusted while maintaining the deposition rate constant.

When a pure 13.56 MHz rf potential is capacitively coupled to the sputter target cathode, a negative dc self-bias potential, V_t, develops at the target, as sketched in Fig. 4-2. The plasma potential, V_{pl}, will be slightly positive relative to the grounded chamber walls, and if the substrate potential, V_s, is allowed to float, it will be more negative than the plasma.

The sputtering rate will depend on the ion current to the target (related to the plasma density) and the target sheath potential, $V_{pl} - V_t$, since the sputtering rate increases with ion energy. The value of the target sheath depends mainly on the electron distribution function and

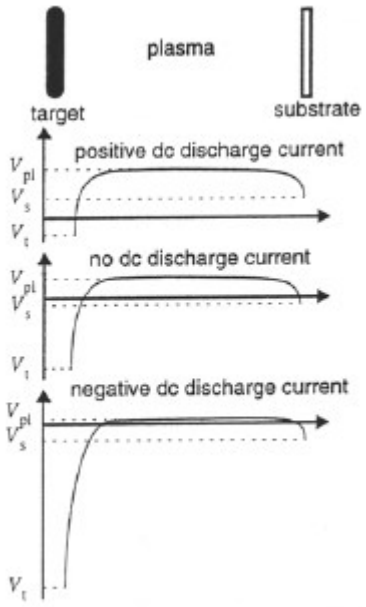

Fig. 4-2: Sketch of potential distribution between sputter target and substrate for different ratios of rf/dc powers.

on the secondary electron emission caused by the ions bombarding the target. Applying to the target a potential different from the normal rf floating potential will create a mixed rf and dc discharge. For a more negative dc potential, the target receives an additional negative current from the external dc bias which will be balanced by an increased (positive) ion current to the target from the plasma and an increase of the secondary electron emission from the target into the plasma due to the higher ion energy. The plasma potential does not follow changes of the target potential since it is controlled by the potential of the much larger non-powered electrode, the chamber walls. This means that the more negative potential of the target results in a higher target sheath, $V_{pl} - V_t$. (See Fig. 4-2) In principle one can gradually change the character of the discharge from pure rf to pure dc by going to a more negative target potential and reducing the rf power. But for insulating targets like CdTe, a pure dc discharge cannot be established because the target surface charges up positively and the discharge extinguishes.

To characterize a superposed rf and dc discharge one should specify the rf power and the potential of the target surface. Unfortunately this potential cannot be measured since any potential probe would interact with the discharge. We can only measure the potential at the back side of the target. This is the potential of the target surface plus the potential drop within the target. The resistivity of the target is a function of target thickness and temperature and changes during deposition. For this reason we do not control the target voltage. Instead we control the dc current which is a monotonic function of $V_{pl} - V_t$ and independent of target conditions. For a negative dc target current the deposition rate can be kept constant by reducing the rf power. For the case of a positive dc current, the potential applied to the target will be less negative than the floating potential and an increased rf power is necessary to keep a constant deposition rate. The relationship we found between rf power and dc current for constant CdTe growth rate is shown in Fig. 4-3.

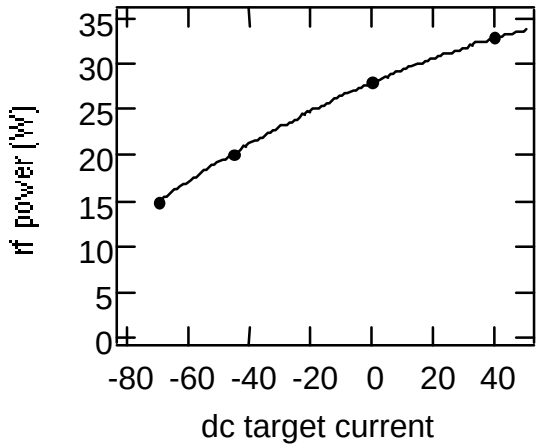

Fig. 4-3: Rf power vs. dc current for discharges yielding a deposition rate of 0.55 nm/s.

Influence of the plasma on the film growth--The *substrate* sheath, $V_{pl} - V_s$ controls the energy of ions which impact the growing film (See Fig. 4-2). The plasma density, in addition to controlling the sputtering rate, also affects the ion flux density to the substrate. These ions may influence the film growth depending on their flux and energy. In previous investigations Wendt *et al*., have shown that the ratio of ion flux density, j_i, to the sputtered (neutral) atom flux density, j_n, arriving at the substrate is much higher for rf excitation of a magnetron sputtering discharge than for dc excitation for the same deposition rate. Thus the ratio of ion to sputtered atom flux can be changed by mixing rf and dc excitation. For a discharge with a balanced magnetron at 50 W discharge power and a pressure of 0.8 Pa, Wendt, *et al*., found a j_i/j_n -ratio of 0.77 and 7.5 for the dc and rf discharges respectively. Some additional results comparing rf and dc discharges are given in [4.8].

The ions arriving at the substrate gain their energy within the substrate sheath potential drop in front of the substrate. This potential drop is higher if rf excitation is used instead of dc excitation. Wendt *et al*. found that at 50 W of discharge power into a three-inch ZnO:Al magnetron target, the average Ar^+ ion kinetic energy incident on a floating substrate was ~16 eV for dc sputtering and ~30 eV for rf sputtering at a pressure of 0.8 Pa. The present study was done under similar conditions, namely, with two-inch magnetrons and 28 W of rf power at 2.4 Pa. Note that the *substrate* sheath potential is greater for rf sputtering whereas the *target* sheath potential is greater for dc sputtering.

In conclusion the energy of ions bombarding the substrate and the ion-to-neutral flux ratio both decrease when switching from a positive to a negative dc discharge current as long as the deposition rate is held constant by adjusting rf power. It should be pointed out that the film growth may be affected by other effects dependent on plasma density such as the electron flux onto the substrate, the degree of dissociation of molecules in the plasma, and an increased substrate temperature due to the energy transferred from the plasma to the substrate. But we believe these are minor compared to the ion bombardment effects.

In Fig. 4-4 the PL data of as-grown CdTe films deposited under three different target bias conditions are shown. We find a clear dependence of the intensity of the broad deep-level PL band centered at about 840 nm (1.48 eV) on the target biasing conditions. For -70 mA this band

is strongest in intensity, decreases when the dc target current is zero during growth, and is almost nonexistent in the case of positive target current. Fig. 4-5 compares the PL of the 1.54 eV band

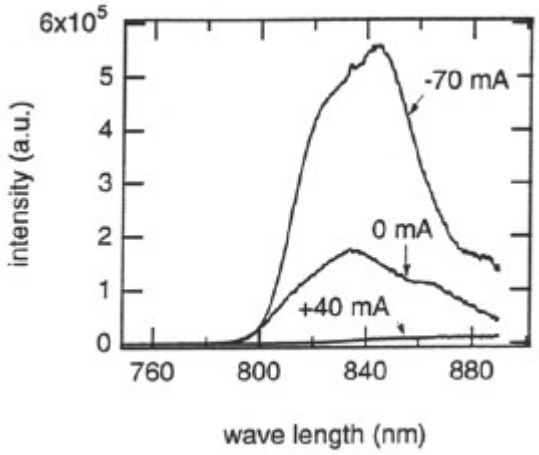

Fig. 4-4: 10K PL spectra of of as-deposited CdTe films excited and observed from the CdTe-air surface (632 nm excitation).

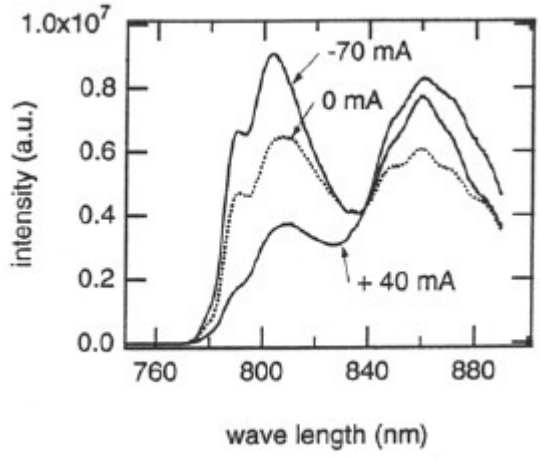

Fig. 4-5: 10K PL spectra of of as-deposited CdTe films excited and observed from the CdTe-air surface of a cell but outside the metallized contact area. Cells received $CdCl_2$ deposition by PLD and 370°C anneal in air.

for the cells (after treatment with $CdCl_2$ and annealing). Again the intensity is strongest if CdTe is deposited under a negative bias current of -70 mA and reduces to about one third for a current of +40 mA. The difference between the PL of the as-grown CdTe films and the solar cells can be attributed to the recrystallization of the CdTe film during the annealing after the $CdCl_2$ deposition. The $CdCl_2$ is known to diffuse into the CdTe during this step and to enhance the crystallization. However it should be noted that the PL indicates that some of the differences observed in as-grown films persists through the $CdCl_2$ treatment steps.

For each solar cell of the 36 cells prepared on one substrate, an IV-curve was taken under one sun illumination. Four cells with the highest efficiencies from each run are compared in terms of fill factor, open circuit voltage and short circuit current in Figs. 4-6, 4-7, and 4-8. Initial efficiencies of more than 12% are found for cells with a target current of -70 mA during the CdTe deposition whereas for a positive target current or +45 mA, the best efficiencies were 9%.

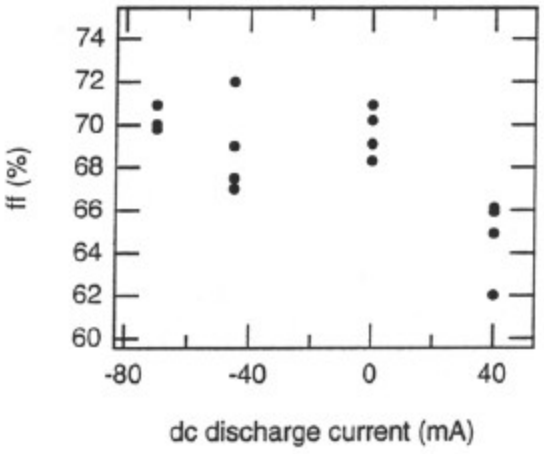

Fig. 4-6: Fill factor of the four cells with the highest efficiencies of each anneal temperature.

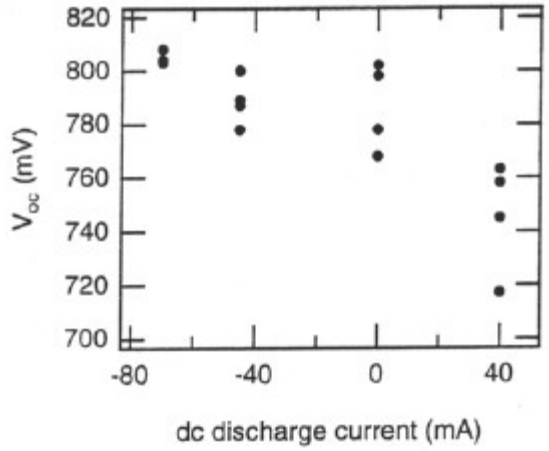

Fig. 4-7: V_{OC} of the four cells with the highest efficiencies of each anneal temperature.

It should be noted that the solar cell performance and the PL probe different regions. The solar cell performance is more sensitive to the CdS/CdTe interface whereas the PL is probed at theCdTe/air interface. (At 633 nm, the absorption length in CdTe is ~0.14 μm.) However results of both methods indicate that a lower plasma density during deposition of the CdTe results in better electronic film properties.

The *in situ* optical transmission results of Fig. 4-9 show significant thin film interference effects which vary with dc current, implying that the film sputtered with a target current of -70 mA has a rougher surface even at early stages of growth. Conversely, the film sputtered with +45 mA has a smoother surface and deeper interferences. These inferences from *in situ*

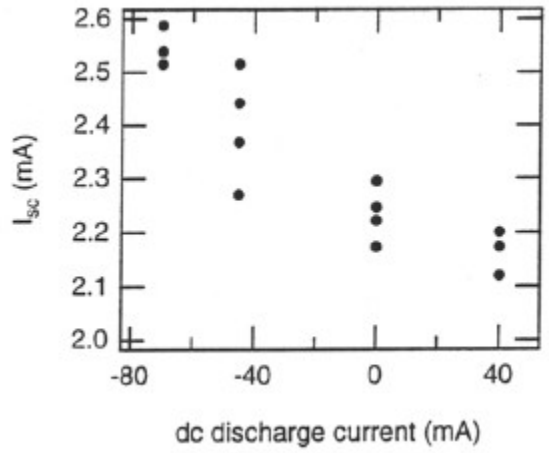

Fig. 4-8: I_{SC} of the four cells with the highest efficiencies of each anneal temperature.

measurements agree well with our SEM images from as-grown films. The film sputtered with +40 mA target current showed flat, top facets larger than those from the film sputtered with -70 mA. Similarly, SEM micrographs of fracture cross sections showed long, nearly continuous columnar grains at –70 mA but at +40 mA discontinuous grain growth. We infer that excessive ion bombardment at +40 mA conditions may be interrupting the grain growth. This is qualitatively consistent with the Monte Carlo simulations of Mueller [4.9] which show that a higher ion flux density or a higher ion energy results in a denser film.

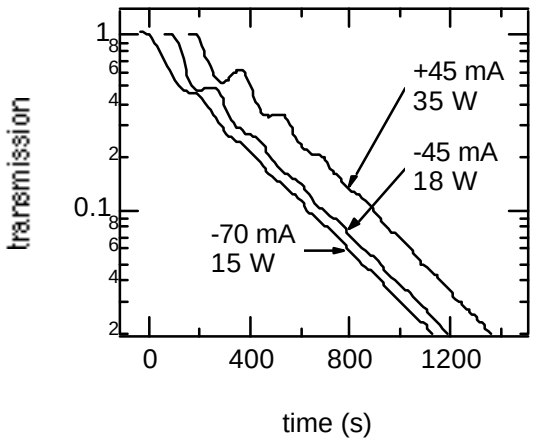

Fig. 4-9: 660 nm *in situ* transmission during deposition of CdTe for three different rf powers and dc currents. Deposition starts at 0, 100 s, and 200 s respectively.

The higher cell performance obtained when CdTe films were sputtered with -70 mA of dc current is consistent with a film having a more columnar structure. This columnar structure apparently also survives the $CdCl_2$ treatment and anneal. Thus, in the solar cell, better current collection would result from fewer transverse grain boundaries to impede the current flow from the CdS/CdTe junction to the back Cu/Au contact.

How might this be connected to the deposition conditions? The -70 mA of dc current and 15 W of rf power result in reduced plasma density. The lower plasma density produces both a lower ion flux to the substrate and a lower substrate sheath potential. One or perhaps both of these conditions improves the film growth. Probably the ion energy is high enough in the case of the 35 W of rf power and +40 mA of dc that damage occurs to the film growth interface which may even interrupt the grain growth. The greatly reduced PL signals from pure rf and almost nonexistent PL from the +40 mA as-grown films also point to ion-induced damage.

It should be noted that the lower plasma density and lower substrate sheath potential at ~70 mA would be expected to *reduce* the heating of the substrate caused by electrons and ions from the plasma and lead to less faceting. This is opposite to what we observe. In addition, we have measured the substrate heating induced by 35 W of rf power to be only 30 ^{o}C so the effects are expected to be small for the changes we have used here.

From the PL we conclude that the excessive ion bombardment which apparently occurs at +45 mA dc and 35 W of rf power, quenches the radiative recombination. The exact origin of the observed photoluminescence bands is uncertain, but similar spectra to those in Fig. 4-5 are reported by Tang *et al*. for fully processed cells [4.10].

The increase in solar cell efficiency with increasing negative dc current is partially due to a higher open circuit voltage (Fig. 4-7) but is mostly due to an increased short circuit current (Fig. 4-8). The higher short circuit current is expected for the film with the more columnar structure. We infer that the plasma conditions at -70 mA dc and 15 W of rf power are the closest to optimum occurring within the range of parameters studied.

References

4.1 R.W. Birkmire, H. Hichri, R. Klenk, M. Marudachalam, B.E. McCandless, J.W. Phillips, J.M. Schulz, and W.N. Shafarman, *13th NREL Photocoltaics Program Review* (AIP Conf. Proc. #353), ed. By H.S. Ullal, and C.E. Witt, pp. 420-27 (1995).

4.2 R. Wendt, K. Ellmer, K. Wiesemann, J. Appl. Phys. **82**, 2115 (1997).

4.3 L. Hultman, J.-E. Sundgren, J.E. Greene, D.B. Bergstrom, I. Petrov, J. Appl. Phys. **78**, 5395 (1995).

4.4 B. Window, N. Savvides, J. Vac. Sci. Technol. A **4**, 196 (1986).

4.5 B. Window, N. Savvides, J. Vac. Sci. Technol. A **4**, 453 (1986).

4.6 J.A. Thornton in Deposition Technologies for Films and Coatings, Noyes Park Ridge, NJ, USA (1982) p. 170.

4.7 S. L. Rohde in Plasma Sources for Thin Film Deposition and Etching, ed. M.H. Francombe, J.L. Vossen, Academic Press, NY, USA (1994) p. 235.

4.8 K. Ellmer, R. Wendt, Surf. Coat. Techn. **93**, 21 (1997).

4.9 K.-H Müller, Phys. Rev. B **35**, 7906 (1987).

4.10 C.W. Tang, F. Vazan, J. Appl. Phys. **55**, 3886 (1985).

5.0 Teaming activity

5.1 Rf sputtered cells on TiO_2-coated substrates/and GPI substrates

We have participated with other members of the national CdTe Team and the Thin Film Partnership Program in studies of resistive layers on conductive SnO_2. Two types of samples were addressed in this study. The first were samples based on Corning 7059 borosilicate glass with a conductive SnO_2 deposited by CVD at the University of South Florida by Chris Ferekides' group and then with an insulating layer of TiO_2 deposited at Harvard by Roy Gordon's group. The second set of samples were deposited on substrates from Golden Photon which had a top layer of "high resistivity" tin oxide on a standard LOF SnO_2:F substrate. The results were summarized by Chris Ferekides at the Teaming meeting held at the Florida Solar Energy Center in Cocoa, FL on January 15-16, 1998. Here we present three tables which summarize the data from the four teams which participated. (These tables are simply re-formatted from those presented at the January 16 Teaming Meeting and also appear in the notes which followed the meeting.)

It should be noted that, although the UT-fabricated cells on the TiO_2 and TiO_2:Nb coated substrates show high V_{OC}, (as high as 830 mV for no CdS layer!) the fill factors are low. The explanation of these two characteristics comes from the shape of the I-V curve which shows a serious “roll-over” in forward voltage near I = 0. (I-Vs were provided in the notes of the meeting.) Apparently there is a back diode at the interface between the CdTe and the titanium dioxide for no CdS, and somewhere between the titanium dioxide and CdS/CdTe interfaces for the cases of 300 Å of CdS and above. Thus, we judge this high V_{OC} to be caused by spurious effects.

TABLE 5.1 - CELLS FABRICATED ON 7059/USF-TO/TiO_2 SUBSTRATES

	Sample ID#	CdS t (A)	Effic. (%)	Voc, (mV)	Jsc, (mA/cm^2)	FF, (%)
IEC	41032.13-2{PRIVATE}41032.12-3	300 1300	1.74 4.98	471 844	14 19.33	26.4 30.5
NREL	T1-c T2-c T3-c T4-c	0 300 800 1600	1.22 6.67 5.06 5.71	760 950 820 770	10.79 24.50 22.08 21.84	14.90 28.67 27.97 33.93
USF	12-10B-4E 12-10B-2D 12-10B-3D	0 600 850	2.32 7.61 9.16	909 833 840	19.35 21.44 20.45	13.20 42.60 53.30
UT	664.5 663.2 662.19 661.6	0 300 1000 2000	0.69 3.95 3.54 2.64	830 800 760 770	9.47 19.36 17.07 14.31	8.72 25.52 27.27 23.93

TABLE 5.2 - CELLS FABRICATED ON 7059/USF-TO/TiO_2:Nb SUBSTRATES						
	Sample ID#	**CdS t (A)**	**Effic. (%)**	**Voc, (mV)**	**Jsc, (mA/cm^2)**	**FF, (%)**
IEC	41032.21-3	300	2.49	620	9.62	41.8
	41032.11-2	1800	3.96	698	17.79	31.9
NREL	T5-c	0	2.92	610	22.56	21.22
	T6-c	300	10.39	740	27.41	51.23
	T7-c	800	9.81	760	23.74	54.35
	T8-c	1600	8.95	750	23.51	50.76
USF	12-10A-2F	850	9.53	788	20.40	59.30
	12-10A-3D	650	9.08	792	18.71	61.30
	12-10A-4D	400	9.23	808	20.39	56.00
	12-10A-1F	0	4.02	578	19.86	35.00
UT	668.14	0	3.34	580	18.71	30.8
	669.21	300	1.82	702	15.3	16.9
	667.12	1000	6.48	810	18.73	42.7

TABLE 5.3 - CELLS FABRICATED ON LOF/GPI-TO SUBSTRATES						
	Sample ID#	**CdS t (A)**	**Effic. (%)**	**Voc, (mV)**	**Jsc, (mA/cm^2)**	**FF, (%)**
IEC	41033.23-6	400	11.56	715	25.1	64.4
	41033.32-1	1500	12.64	795	21.57	73.7
NREL	T9-a	0	9.12	780	21.19	55.19
	T10-b1	300	11.27	790	22.71	62.81
	T11-c2	800	11.14	770	21.40	67.64
	T12a	1600	8.92	780	17.19	66.55
USF	12-10A-14B	400	12.23	828	21.33	69.24
	12-10A-13F	550	11.46	811	20.76	68.05
	12-10A-11C	750	10.50	831	19.22	65.77
	12-10A-12E	850	10.30	776	19.63	67.61
UT	668.12	0	6.34	660	17.07	56.25
	663.12	300	9.47	800	20.43	57.94
	667.3	1000	11.21	820	20.43	66.92
	660.8	1500	8.90	770	18.71	61.81
USF-2	12-10B-11E	200	12.02	812	21.49	68.89
	12-10B-12D	400	11.42	815	20.50	68.36

5.2 Electrical measurements of GPI HR-SnO_2

Peter Meyers and Scot Albright of ITN have provided us with a sample of the Golden Photon high resistivity tin oxide (HR-SnO_2) deposited on borosilicate glass. Randy Bohn has performed electrical measurements on this sample with the following results:

The electrical conductivity of the Golden Photon sample film was measured from 275K to 350K and showed an activation energy-like behavior with respect to temperature. The measurement was repeated and an activation energy of 0.106 eV was found for this temperature range. These measurements were extended down to 80K and it was found that between 80K and 350K a single activation energy could not describe the conductivity. However, a model with two activation energies could be used to describe the conductivity:

$$\sigma = Ae^{-E1/kT} + Be^{-E2/kT}$$

Here E1 = 0.104 eV and E2 = 0.034 eV. At least one model [5.1] in the literature relates these energies to carrier traps and argues that the conductivity activity energy is a measure of the trap energy relative to the conduction band. This model also proposes that the pre-factor is very roughly inversely proportional to the trap density. Here A = 0.24 and B = 0.00135 which suggests that the trap density is about 100 times higher for the traps at 0.034 eV.

The conductivity of this Golden Photon film is markedly different from the typical LOF tin oxide substrate whose conductivity is essentially temperature independent over this same temperature range (a degenerate semiconductor) and 5 orders of magnitude higher.

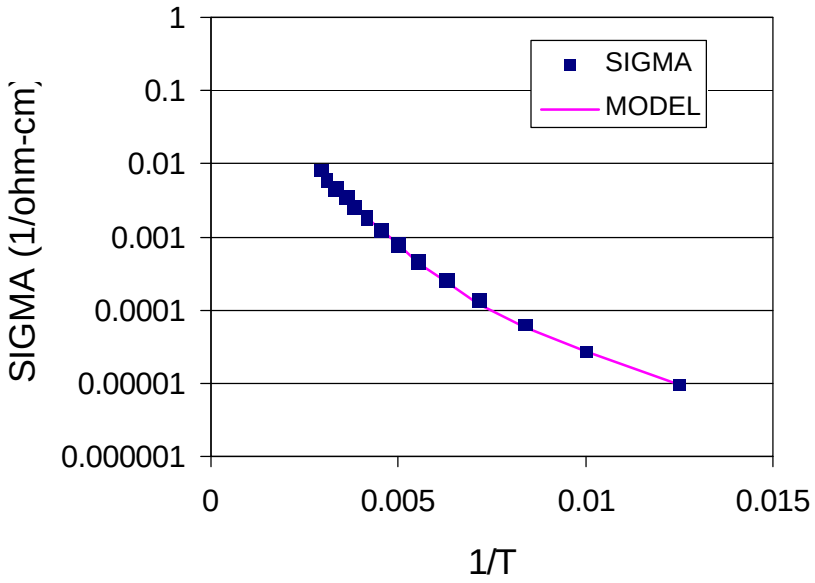

Fig. 5-1: Electrical conductivity (sigma) vs. temperature for HR-tin oxide from Golden Photon.

Reference

5.1 J. W. Orton and M.J. Powell, Rep. Prog. Phys. **43**, 1263 (1980)

6.0 Undergraduate projects

6.1 NSF REU Program

In the summer of 1997, Kathy Jude participated in our PV projects with an emphasis on doing spectral quantum efficiency measurements and making improvements to the system. Kathy, a physics major from the University of West Virginia, was supported in part by the NSF grant, Research Experiences for Undergraduates to the Department of Physics and Astronomy of The University of Toledo. The abstract of her report follows:

> The spectral quantum efficiency of CdS/CdTe thin film solar cells was measured using a monochromator to separate the spectrum of light focused on the solar cell. The current generated by the cell was calculated by measuring the voltage drop across a 10 ohm resistor connected to a lock-in detector and a Philips meter. The spectral quantum efficiency was then computed by comparison to a UDT-20 silicon cell whose SQE curve is known. Results were obtained and analyzed for several cells fabricated by Dr. Al Compaan's group at the University of Toledo..

6.2 Senior honors project

Undergraduate student Martin Hardin from the UT College of Engineering was advised by Prof. Compaan in his senior Engineering Physics project. This was a design and construction project for a vapor $CdCl_2$ treatment/annealing system. The results of this project have been described in Section 4.1 above. The title of his report is "Cadmium Chloride Vapor Treatment of Cadmium Telluride Photocells."

7.0 Conclusions and Acknowledgements

7.1 Conclusions

The resistivity of the CdS_xTe_{1-x} alloys grown by PLD shows a strong compositional dependence changing by almost eight orders of magnitude as x varies from 0 to 1. This change appears to be due to a change in carrier density. The activation energy for the resistivity increases as x decreases which suggests the possibility of an increase in the effective trap depth. Annealing increases the resistivity of the S-rich films, and also increases the dark-to-light ratio of the resistivity suggesting the removal of defects. A preliminary study of persistent photoconductivity in selected films seems to support this premise showing a decrease in the decay time constant after annealing.

A line shape study of LO Raman lines of the CdS-like LO phonons shows a composition dependence of the phonon coherence lengths for the CdS_xTe_{1-x} alloy system. Films with x outside the miscibility gap show coherence lengths of up to 15 lattice constants while alloys with compositions well within the miscibility gap have coherence lengths down to 7.5 lattice constants. The phonon frequency at the zone center, $\omega_o(x)$, has been inferred for each alloy and found to be up to 5.1 cm^{-1} higher than $\omega_{max}(x)$, the observed Raman peak position, for the alloy with x=0.41.

Using an x-dependent Warren-Cowley short-range order parameter, a composition-dependent average cluster length has been calculated which agrees with the observed phonon coherence lengths. Thus we have shown how the Raman lineshape and asymmetry resulting from phonon confinement or spatial correlation effects can yield a microclustering probability. This short-range ordering is strong in the case of the CdS_xTe_{1-x} alloy system with its large miscibility gap.

Studies of inverted (glass/CdTe/CdS) heterojunctions using ADXRF show that after thermal annealing there is a redistribution of both Cd and Te atoms. The heat treatment tends to reduce the original Te concentration contrast between CdS and CdTe layers and results in a blurred junction. When the annealing temperature exceeds a certain critical value (370°C in our samples) an inverted junction can be transformed into a complicated admixture behaving like a normal junction near the surface of CdS, as manifested by a Te/Cd concentration ratio higher than that in the second (CdTe) layer. In a separate experiment we have found that the interfacial roughness at the CdS/CdTe interface also changes significantly with annealing temperature in these heterojunctions. These results of *nondestructive* characterization of heterojunctions using ADXRF could therefore serve as useful tools for the control of atomic intermixing in the growth of thin film photovoltaic materials. These results were confirmed using a normal cell structure showing an improved short-circuit current and efficiency for cells annealed above 380°C.

A new vapor $CdCl_2$ system has been constructed which allows better control of gas flow and temperature during the annealing process. This new system also has the advantage of a computer-controlled annealing cycle.

We have also investigated the potential for the use of a combined rf and dc excitation of the sputtering cathode during CdTe deposition. It would appear that the energy of ions bombarding the substrate and the ion-to-neutral flux ratio both decrease when switching from a positive to a negative dc discharge current as long as the deposition rate is held constant by adjusting rf power. The film growth may be influenced by other factors dependent on plasma density such as the electron flux onto the substrate, the degree of dissociation of molecules in the

plasma, and an increased substrate temperature due to the energy transferred from the plasma to the substrate. We believe these are minor compared to the ion bombardment effects.

Teaming activities continued with a focus on cells grown on high resistivity layers on conducting tin oxide. The conductivity of a substrate from Golden Photon was measured from 80K to 350K and the results could not be described using a model with a single activation energy.

7.2 Future Directions

We plan to continue to optimize the rf and rf+dc sputter deposition processes for the CdS and CdTe layers with the goal of achieving higher cell efficiencies. An assessment of how processing changes of deposition rate, CdTe layer thickness, and processing times might apply to manufacturing plant throughput and how these changes might affect device performance will also be undertaken. Laser patterning experiments will also be undertaken in an effort to develop CdTe mini-modules (~30 cm^2). In cooperation with the national sub-team on CdTe performance and stability, we plan to develop bias stress testing capabilities and to begin studies of degradation processes relevant to predicting the long-term performance of CdTe modules.

We will continue to carry out our cell and material characterization studies to support the UT cell fabrication efforts and to continue our role as part of the national teaming effort. The following techniques will be used as needed to study cells and materials (including intermixing and transition layers between materials): low temperature photoluminescence (PL), Raman spectroscopy, Hall and photo-Hall measurements, Rutherford backscattering, grazing incidence x-ray scattering, and optical absorption. Device performance will be assessed from current-voltage and quantum efficiency measurements

We plan to also address the window layer and the question of the back contact. This will include the possibility of using ZnO:F and possibly ZnO:Al as a TCO window and the use of sputtering for deposition of intrinsic and/or doped SnO_2. We will also explore reactive sputtering processes where applicable (e.g., SnO_2 with oxygen, CdTe:N, and ZnTe:N). Because of our experience with the CdS/CdTe alloy films, we are in a position to assess the effects of intermixing and of transition layers on the front and rear junction of the cells. This also could be applied to the study of optimization schemes such as anti-reflection coatings, multi-layer TCO's, and graded-gap CdSTe layers.

7.3 Acknowledgments

Many individuals, in addition to those at the University of Toledo, have contributed to this work over the past year. This includes many at Solar Cells, Inc., especially Gary Dorer and Upali Jayamaha. Our collaborations with Dave Albin, Ramesh Dhere, Chris Ferekides, Roy Gordon, Brian McCandless, Lawrence Anthony, and members of the teaming activity have led to much of the success that we have had with this project during the past year. We would like to thank LOF for the supply of superstrate material. Finally, we are especially grateful to our contract monitor, Bolko von Roedern, for his helpful suggestions.

8.0 Publications

Refereed papers published or in press

1. A. Fischer, D. Grecu, E. Bykov, R.G. Bohn, and A.D. Compaan, "Raman and RBS Studies of Interdiffusion in RF Sputtered CdS/CdTe Solar Cells," NREL/SNL Photovoltaics Program Review--Proceedings of the 14th Conference, ed. by C.E. Witt, M. Al-Jassim, and J.M. Gee (AIP Conference Proceedings No. 394) (1997), pp. 655-664.

2. A. Fischer, Z. Feng, E. Bykov, G. Contreras-Puente, A. Compaan, F. Castille-Alvarado, J. Avendano, and A. Mason, "Optical phonons in laser-deposited CsS_xTe_{1-x} films," Appl. Phys. Lett. **70**, 3239-41 (1997).

3. A.D. Compaan, R.G. Bohn, A. Fischer, R. Wendt, D. Grecu, E. Bykov, X. Deng, C. Narayanswamy, D. Zuo, X. Ma, and K. Makhratchev, "High Efficiency Thin-Film Cadmium Telluride Photovoltaic Cells", subcontract report published in Annual Report, Photovoltaic Subcontract Program, FY1997 [available from NTIS: publication NREL/SR-520-23404 (8/97)].

4. A.D. Compaan, R.G. Bohn, U. Jayamaha, A. Fischer, D. Grecu, E. Bykov, C. Narayanswamy, and D. Zuo, "High Efficiency Thin Film Cadmium Telluride Photovoltaic Cells," Annual Report, NREL Photovoltaic Program, FY 1996, [available from NTIS: publication NREL/TP-451-21233 (5/96)].

5. A. Fischer, X. Deng, D. Grecu, K. Makhratchev, X. Ma, R. Wendt, D. Zuo, A.D. Compaan and R.G. Bohn, "Properties of CdS_xTe_{1-x} Alloy Films," 26th IEEE Photovoltaic Specialists Conference-1997, pp. 447-450.

6. A. Fischer, L. Anthony and A.D. Compaan, "Raman Analysis of Short-Range Clustering in Laser-Deposited CdS_xTe_{1-x} Films," Appl. Phys. Lett. **72**, 2559 (1998)

7. M. Tufino-Velazquez, G. Contreras-Puente, M.L. Albor-Aguilera, M.A. Gonzalez-Trujillo, and A.D. Compaan, "Thin Film Solar Cell Heterojunctions Deposited by rf Planar Magnetron Sputtering and HW-CSVT" to appear in *Proc. of the 14th Photovoltaics Solar Energy Conference of Europe* (Barcelona, Spain-1997)

8. Y.L. Soo, S. Huang, Y.H. Kao, and A.D. Compaan, "Investigation of interface morphology and composition mixing in CdTe/CdS heterojunction photovoltaic materials using synchrotron radiation," J. Appl. Phys. **83**, 4173 (1998).

9.0 Project personnel

Yevgeniy Bykov	"Capacitive Measurements for Quantitative Analysis of Sputtered CdTe Solar Cells" (M.S., March 1997)
Xiangdong Deng	"Electrical Properties of Semiconductor Thin Film CdS_xTe_{1-x} Grown By Laser Physical Vapor Deposition" (M.S., August 1997)
David Zuo	" Optical Absorption of CdS_xTe_{1-x} Alloy Films at 10K" (M.S., December 1997)
Dan Grecu	Ph.D. in progress
Xianda Ma	Ph.D. in progress
Konstantin Makhratchev	M.S. in progress
Ilvydas Matulionis	Ph.D. in progress
Shogo Nakade	M.S. in progress
Diana Shvydka	Ph.D. in progress
Dr. Andreas Fischer	Postdoctoral associate (December 1996—June 1997)
Dr. Ralf Wendt	Visiting postdoctoral associate (March-May 1997)

REPORT DOCUMENTATION PAGE

Form Approved
OMB NO. 0704-0188

Public reporting burden for this collection of information is estimated to average 1 hour per response, including the time for reviewing instructions, searching existing data sources, gathering and maintaining the data needed, and completing and reviewing the collection of information. Send comments regarding this burden estimate or any other aspect of this collection of information, including suggestions for reducing this burden, to Washington Headquarters Services, Directorate for Information Operations and Reports, 1215 Jefferson Davis Highway, Suite 1204, Arlington, VA 22202-4302, and to the Office of Management and Budget, Paperwork Reduction Project (0704-0188), Washington, DC 20503.

1. AGENCY USE ONLY (Leave blank)	2. REPORT DATE	3. REPORT TYPE AND DATES COVERED
	November 1998	Final Technical Report, 21 January 1994–31 March 1998

4. TITLE AND SUBTITLE
High-Efficiency Thin-Film Cadmium Telluride Photovoltaic Cells; Final Subcontract Report, Final Technical Report, 21 January 1994–31 March 1998

5. FUNDING NUMBERS
C: ZAX-4-14013-4
TA: PV905001

6. AUTHOR(S)
A.D. Compaan and R.G. Bohn

7. PERFORMING ORGANIZATION NAME(S) AND ADDRESS(ES)
Department of Physics and Astronomy
The University of Toledo
Toledo, OH 43606

8. PERFORMING ORGANIZATION REPORT NUMBER

9. SPONSORING/MONITORING AGENCY NAME(S) AND ADDRESS(ES)
National Renewable Energy Laboratory
1617 Cole Blvd.
Golden, CO 80401-3393

10. SPONSORING/MONITORING AGENCY REPORT NUMBER
SR-520-25856

11. SUPPLEMENTARY NOTES
NREL Technical Monitor: B. von Roedern

12a. DISTRIBUTION/AVAILABILITY STATEMENT
National Technical Information Service
U.S. Department of Commerce
5285 Port Royal Road
Springfield, VA 22161

12b. DISTRIBUTION CODE

13. ABSTRACT *(Maximum 200 words)*

This report describes work performed during the past year by The University of Toledo photovoltaics group. Researchers continued to develop rf sputtering for CdS/CdTe thin-film solar cells and to optimize the post-deposition process steps to match the characteristics of the sputtering process. During the fourth phase of the present contract, we focused on determining factors that limit the efficiency in our "all-sputtered" thin-film CdTe solar cells on soda-lime glass. These issues include controlling CdS/CdTe interdiffusion, understanding the properties of the CdS_xTe_{1-x} alloy, optimizing process conditions for $CdCl_2$ treatments, manipulating the influence of ion bombardment during rf sputtering, and understanding the role of copper in quenching photoluminescence and carrier lifetimes in CdTe. To better understand the important CdS/CdTe interdiffusion process, we have continued our collaboration with the University at Buffalo and Brookhaven National Synchrotron Light Source in measurements using grazing-incidence X-rays. Interdiffusion results in the formation of the ternary alloy material CdS_xTe_{1-x} at or near the heterojunction, where its properties are critical to the operation of the solar cell. We have placed significant effort on characterizing this alloy, an effort begun in the last phase. A complete set of films spanning the alloy range, prepared by pulsed-laser deposition, has now been characterized by wavelength dispersive X-ray spectroscopy and optical absorption at NREL; by Raman scattering, X-ray diffraction, and electrical measurements in our lab; and by spectroscopic ellipsometry at Brooklyn College. We continued to participate in cooperative activity with the CdTe National Team. We prepared a series of depositions on borosilicate glass substrates having doped SnO_2 layers coated with TiO_2 (prepared by the University of South Florida and Harvard) and similar substrates having a resistive SnO_2 layer on the doped tin oxide (fabricated by Golden Photon). The Golden Photon high-resistivity SnO_2 structure yielded excellent cell performance.

14. SUBJECT TERMS	15. NUMBER OF PAGES
photovoltaics ; high-efficiency thin films ; cadmium telluride ; rf sputtering ; ion bombardment	49
	16. PRICE CODE

17. SECURITY CLASSIFICATION OF REPORT	18. SECURITY CLASSIFICATION OF THIS PAGE	19. SECURITY CLASSIFICATION OF ABSTRACT	20. LIMITATION OF ABSTRACT
Unclassified	Unclassified	Unclassified	UL